INFORMATION TO USERS

This manuscript has been reproduced from the microfilm master. UMI films the text directly from the original or copy submitted. Thus, some thesis and dissertation copies are in typewriter face, while others may be from any type of computer printer.

The quality of this reproduction is dependent upon the quality of the copy submitted. Broken or indistinct print, colored or poor quality illustrations and photographs, print bleedthrough, substandard margins, and improper alignment can adversely affect reproduction.

In the unlikely event that the author did not send UMI a complete manuscript and there are missing pages, these will be noted. Also, if unauthorized copyright material had to be removed, a note will indicate the deletion.

Oversize materials (e.g., maps, drawings, charts) are reproduced by sectioning the original, beginning at the upper left-hand corner and continuing from left to right in equal sections with small overlaps.

Photographs included in the original manuscript have been reproduced xerographically in this copy. Higher quality 6" x 9" black and white photographic prints are available for any photographs or illustrations appearing in this copy for an additional charge. Contact UMI directly to order.

ProQuest Information and Learning
300 North Zeeb Road, Ann Arbor, MI 48106-1346 USA
800-521-0600

UMI®

Fluorescence Anisotropy Near-Field Scanning Optical Microscopy (FANSOM): A New Technique for Biological Microviscometry

By

Frederick B. Reitz

A dissertation submitted in partial fulfillment
of the requirements for the degree of

Doctor of Philosophy

University of Washington

2001

Program Authorized to Offer Degree: Department of Bioengineering

UMI Number: 3014108

Bell & Howell Information and Learning Company
300 North Zeeb Road
P.O. Box 1346
Ann Arbor, MI 48106-1346

Doctoral Dissertation

In presenting this dissertation in partial fulfillment of the requirements for the Doctoral degree at the University of Washington, I agree that the Library shall make its copies freely available for inspection. I further agree that extensive copying of the dissertation is allowable only for scholarly purposes, consistent with "fair use" as prescribed in the U.S. Copyright Law. Requests for copying or reproduction of this dissertation may be referred to Bell and Howell Information and Learning, 300 North Zeeb Road, P.O. Box 1346, Ann Arbor, MI 48106-1346, to whom the author has granted "the right to reproduce and sell (a) copies of the manuscript in microform and/or (b) printed copies of the manuscript made from microform."

Signature________________________________

Date 3/8/01

University of Washington
Graduate School

This is to certify that I have examined this copy of a doctoral dissertation by

Frederick B. Reitz

and have found that it is complete and satisfactory in all respects,
and that any and all revisions required by the final
examining committee have been made.

Chair of Supervisory Committee:

Gerald Pollack

Reading Committee:

Gerald Pollack

Martin Kushmerick

Barbara Trask

Date: 3/8/01

University of Washington

Abstract

Fluorescence Anisotropy Near-Field Scanning Optical Microscopy (FANSOM): A New Technique for Biological Microviscometry

by Frederick B. Reitz

Chairperson of the Supervisory Committee

Professor Gerald H. Pollack
Department of Bioengineering

To test hypotheses regarding putative roles of water structuring in cell function, a near-field scanning optical microscope system was implemented and adapted for nano-scale fluorescence anisotropy measurement. Technical challenges to be overcome included delivery of polarized light to the sample via a tapered optical fiber, implementation of a suitable shear-force system, choice and design of optimized molecular probes for microviscometry, quantitatively accurate distinction of fluorescence polarization components, and measurement of a small region within a bath of fluorophore. The performance of the system as a near-field microscope and as an accurate monitor of fluorescence anisotropy was verified. Lateral shear force and optical resolutions were found to be 200 nm and 250 nm, respectively, and measured anisotropies in solutions of known viscosity agreed well with theoretical values. When employed in a vertical scanning mode, Z-axis resolution of anisotropy

variations was < 100 µm. Microviscometric results in gels in which water had previously been found to be bound showed a correlation between microviscosity and measured bound fraction (~ 1 cp / 0.3% bound water; $R^2 = 0.7435$). An untreated glass surface and a hydrophobic surface were assayed for induction of microviscometric deviation in the water above them; none was found (detection limit ~ µm and 10 cp in the case of untreated glass, and ~ 30 nm and ~ 0.1 cp in the case of the hydrophobic surface). Water above a cleaved mica surface showed an increased microviscosity over a range of several microns. In its first biological application, the system was used to investigate the triple-banding pattern seen in previous shear-force images of myofibril bundles, showing them to be optical in origin.

TABLE OF CONTENTS

List of Figures....iii

List of Tables....v

1. Introduction....1

2. Background....4
2.1. Near-field Scanning Optical Microscopy (NSOM)....4
2.2. Water structure....5
2.3. Previous NSOM-viscometry work....7
2.4. Fluorescence Anisotropy....9
2.5. Microviscosity....12
2.6. Fluorescence Anisotropy NSOM (FANSOM) feasibility....13
2.6.1. NSOM probe polarization retention....13
2.6.2. Light levels....15

3. The FANSOM system....17
3.1. System overview....17
3.2. Light source and conditioning....17
3.3. Nanopositioning....20
3.4. Probe manufacture....20
3.5. Shear force system....25
3.6. Polarized photodetection....30
3.7. Confocal operation....32
3.8. Fluorophore development and choice....36

4. FANSOM system characterization....44
4.1. Scans of gratings....44
4.2. Preliminary SSFA trials....44
4.3. Z-resolution....52

5. SSFA in gels....59
5.1. SSFA in dense polyacrylamide....59
5.2. SSFA in agarose gels....61

6. FANSOM over putative structuring surfaces

6.1. Glass....66
6.2. Sigmacote®....68
6.3. Cleaved mica....70

7. Biological applications of FANSOM....74
7.1. Scans of myofibril bundles....74

8. Future directions....86
8.1. Instrumentation upgrades....86
8.2. Experimental possibilities....87

References....89

Appendix. SSFA of fluorophores excited by light of a given polarization state...95

LIST OF FIGURES

Number Page

1.1: Current hypotheses....2
2.1: Cantilever vibrational modes....8
2.2: Fluorescence anisotropy....11
3.1: FANSOM optical path....18
3.2: Nanopositioning system....21
3.3: SEM of an etched NSOM probe....22
3.4: Probe assembly gluing jig....24
3.5: Probe resonance spectra in air and water....26
3.6: Shear-force system....27
3.7: Shear-force approach curve....29
3.8: Diagram of confocal assembly....33
3.9: Effect of defocusing on collected light with 200-micron pinhole....35
3.10: Effect of defocusing on collected light with 40-micron pinhole....37
3.11: Comparison of molecular probe designs....40
4.1: Shear-force scan of a 1-micron grating....45
4.2: NSOM scan of a 3-micron grating....46
4.3: Effect of light leakage to parallel PMT channel....49
4.4: Effect of mis-estimation of G....50
4.5: Corrected SSFA calibrations....51
4.6: Immersion-oil approach with cleaved optical fiber vs. NSOM probe....53
4.7: Isooctane approach with cleaved optical fiber vs. NSOM probe....55
4.8: Vertical FANSOM system response....57
5.1: Microviscosity before and after polyacrylamide gelation....60
5.2: Microviscosity as a function of agarose concentration....62

5.3: A simplified model of agarose gel structure....64
6.1: FANSOM over untreated glass....67
6.2: FANSOM over Sigmacote®-treated glass....69
6.3: FANSOM over cleaved mica....72
7.1: Thick myofibril bundle scan of Seibel (1996)....75
7.2: Constant height scanning....77
7.3: Thick myofibril bundle planar scans at varying heights....79
7.4: Thick myofibril bundle planar scan, rotated orientation....80
7.5: Narrow myofibril bundle planar scan....81
7.6: Narrow myofibril bundle planar scan, repeated....82
7.7: Narrow myofibril bundle planar scan, reversed contrast....83

LIST OF TABLES

Number Page

3.1: Comparison of independently determined SSFA values..........................42

4.1: SSFA calibrations..47

Acknowledgements

Special Thanks to -

Gerald Pollack
Eric Seibel
Mark Fauver
Jeff Magula
John Myers
Stephanie Lara
Len Pagliaro
Pedro Verdugo
Christopher Viney
David Burns
Ake Lernmark
Daniel Porte, Jr.
Ed Krebs
Iris Asllani
Jian Wang
Martin Kushmerick
Barbara Trask
Richard Storch
Isabel Landsberg
Sarah Kukhan
Pat Jarvis

In loving memory of

Col. George William Reitz
Annina Bond Reitz
Twila Montez Reitz
Mary Beth Richards
Earl Emmett Richards

1. Introduction

This project comprises the adaptation of a near-field scanning optical microscope for viscometric use and the application of this system to questions regarding water structure.

"Water structure" refers to the tendency of water to self-associate in an ordered fashion, creating islands of structure amidst Brownian chaos. These islands may be fleeting, as is thought to be the case in the bulk, or induced by a dipolar or charged surface. The layer of water closest to such a surface is most strongly adhered and is referred to as the "primary hydration shell", or simply the "water of hydration". The presence of a layer of somewhat immobilized water suggests the possibility of subsequent layers of bound water, similarly partially immobilized as they in turn hydrate the water of hydration. This secondary zone of bound, or "vicinal", water is called the "solvation zone" (Israelachvili, 1992).

How extensive is this hydration zone?

Figure 1.1 graphically shows a sample of standing hypotheses from the literature. The suggested extents of vicinal water range from only one to two water layers (for non-planar surfaces; Israelachvili and Wennerstrom, 1996), to many microns (for biological surfaces; Pollack, 2001), to a range bounded only by the containing vessel (Wiggins, 1990). Other hypotheses address the possible properties of such water, such as increased or decreased viscosity near hydrophobic or hydrophilic surfaces, respectively (Vogler, 1998), reduced solvation of solutes (Hirai), or simply that surface drag effects will occur at near-molecular scales (Howard, 1996).

Semi-quantitative cartoon of current hypotheses

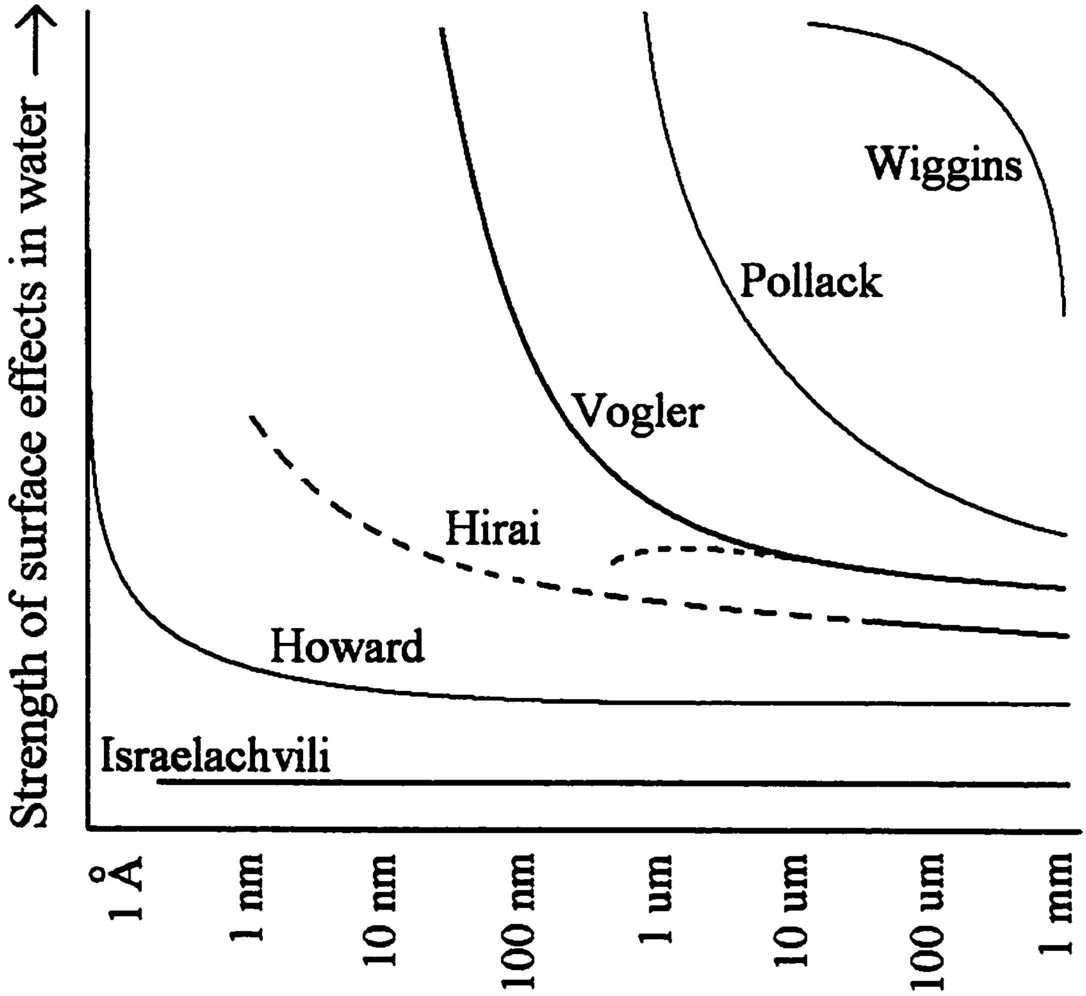

Figure 1.1. Current hypotheses. The effects of surfaces upon the properties of water are currently difficult to measure directly. Opinions regarding the nature and extent of such phenomena vary widely, from neglibility (on non-planar surfaces; Israelachvili and Wennerstrom, 1996) to unbounded structuring (Wiggins, 1990).

Is vicinal water unusually viscous? Do surfaces of differing hydrophilicities modify their immediate environment, and if so, how far does this influence extend?

Also controversial is the nature of the quasi-viscous “shear-force” imaging mode often used over surfaces in conjunction with near-field scanning optical microscopy. Do the features in published images correspond directly to surface features, or to variations in their hydration?

It was with these questions in mind that this project was undertaken.

In Near-field Scanning Optical Microscopy (NSOM), light is “funneled” to, rather than focused upon, the sample under scrutiny, building up a super-resolution image one pixel at a time. Can fluorescent techniques currently used to measure molecular dynamics be combined with this technology, allowing viscometry of sub-micron resolution? Could shear-force imaging be employed to map viscosity?

Given the ubiquity of water, and its inherency to life, an increased understanding of the behavior of water at surfaces could have profound repercussions. Virtually all cellular water is poised within nanometers of a macromolecule, and within angstroms of a solute (Luby-Phelps et al., 1986; Goodsell, 1993). An investigation of such water is described herein.

2. Background

2.1 Near-Field Scanning Optical Microscopy (NSOM)

The foundation upon which the instrumentation described herein was constructed was a largely conventional NSOM system (cf. Betzig et al., 1992; Gheber et al., 1998). As the name suggests, NSOM is an optical microscopy, and as such does not require the fixation or coating of samples as is typical of electron microscopy. Further, NSOM can take advantage of the plethora of fluorescent probes available. The key difference between NSOM and conventional optical microscopy is that in NSOM, the light is "funneled" to the sample rather than focused, allowing sub-diffraction limit control of sample illumination, and thus higher resolution. These characteristics make NSOM particularly promising for application to modern biological research.

The heart of the NSOM system is the "funnel", or "probe" itself. The probe has traditionally been made by heat-pulling an optical fiber in much the same way that capillaries are pulled for electrophysiological or microinjection purposes (Betzig et al., 1992). The goal is a fiber that necks down to a point of ~ 50 nm diameter. The small size of the aperture largely determines the resolution that can be obtained. Current literature typically shows resolution of ~150 nm, with instances of 60 nm or even 10 nm reported (Talley et al., 1996; Cline et al., 1991; Grubb et al., 1994).

The length of the tip is also important because it influences the efficiency of the probe. The longer the stretch of sub-wavelength fiber that the light must evanescently traverse before being coupled out of the probe, the more attenuated the transmitted light will be. Transmission efficiencies of ~ 0.0001% are typical.

More recently, techniques have been developed for the construction of probe tapers by acid etching (Hoffmann et al., 1995; Stockle et al., 1999a; Lambelet et al., 1998a). Because the taper is constructed without otherwise distorting the fiber core, the region of sub-wavelength fiber is minimized, exponentially increasing transmission efficiencies to values as high as 1% (Stockle et al., 1999b).

2.2 Water structure

Water is a dipolar molecule and as such would be expected to be influenced by electrostatic fields, such as those imposed by the presence of ions in solution, charged surfaces, or even other water molecules. But how powerful is this influence? Over what range might it overpower Brownian motion?

The equilibrium angular distribution of molecules in an electric field is given by

$$f(\theta) = Ke^{\mu E \cos\theta / kT}$$

where K is a normalization constant, μ is the dipole moment of the molecule in question, E is the imposed electric field strength, θ is the angle between the molecule's dipole and the electric field, k is the Boltzmann constant, and T is the temperature (van Holde, 1985).

The amount of energy in the interaction of the molecule with the electric field becomes large relative to that of the background of thermal energy when $\mu E > kT$. For a water molecule at room temperature, this condition occurs at a field strength of > 7 MV/cm.

The electric field surrounding an unshielded point charge is given by

$$E = q / 4 \pi \varepsilon_0 r^2,$$

where q is the amount of charge, ε_0 is the permittivity of free space, and r is the distance from the point. In the case of a bare, monovalent ion, a field strength of 7 MV/cm is exceeded upon moving withing 1.2 nm of the ion. Given the linear density of water molecules in liquid water, this distance represents ~ 4 water molecules of depth. The very first layer of molecules, being some 10 times closer to the ion than those at this equipotential surface, experience a field strength 100 times higher than the latter. It must also be considered, however, that the dielectric constant of water at low frequencies is ~ 78, providing significant shielding to molecules situated beyond the foremost layers.

Viscosity can be understood to a first approximation as representing the product of the free energy density of the fluid and the time interval between intermolecular interactions (Witten, 1990). For water, which has ~ 1 centipoise (= 1 dyne • sec / cm^2) of viscosity, these values are ~ 10 kcal/mole (~ 10^{10} dyne / cm^2) and ~ pS, respectively. The attractive energy between water molecules in solution, including both hydrogen bonding and van der Waals forces is ~ 11 kcal/mole, or ~ 19 kT per molecule at room temperature. This value is many times that of the few kT of thermal energy present per molecule (Solomons, 1988). This amount of energy is on the order of, yet slightly smaller than, the entropic cost of ~ 14 kcal/mole involved in immobilizing the water molecules, suggesting partial freedom of motion (cf. Andrews et al., 1984).

Together, these figures suggest a layer or two of quite highly constrained water immediately upon a charged surface, abutted by somewhat dynamic, self-associated, bulk water. To what degree does the bulk water propagate the directionality imposed by the surface? Israelachvilli and others have found that "long range" solvation forces (decay length ~ 1 to 100 nm) can modulate the density of water between surfaces (Israelachvilli and McGuiggan, 1998; Israelachvili and Adams, 1976; Israelachvili and Adams, 1978), suggesting an empirically measured, and therefore lower, bound.

2.3 Previous NSOM-Viscometry work

The currently predominant mechanism for probe-sample distance control is shear force feedback. In shear-force feedback, the NSOM tip is vibrated at a resonance, and this vibration is monitored. As the tip nears the surface, tip-surface interactions measurably perturb the vibration in a distance-dependent manner. This signal can therefore be used for probe-sample distance control. The "shear force" is thought to be in part a viscous phenomenon. Might shear force be employed for high-resolution viscometry?

Viscous drag forces are proportional to velocity, which in turn increases with increasing probe tip displacement. This displacement varies spatially with the harmonic mode in which the cantilevered probe is vibrating. The first three modes of lateral probe vibration are shown in **Figure 2.1**. It is apparent from the figure that the first mode has the highest ratio of tip displacement to average shank displacement, making it a promising choice for the confinement of viscometry to a small voxel. The last 15% of the probe's length, when vibrated in this mode, contributes 50% of the total drag force on the probe. For a 1-mm probe tip, this would correspond to a length of 150 µm. The amplitude of vibration used in shear force techniques is typically small (~ 3 nm at the tip), so lateral resolution would be expected to be approximately that of the average diameter of the probe (~ 100 µm shank tapering down to ~ 100 nm at the tip, weighted by the vibrational amplitude that increases toward the tip).

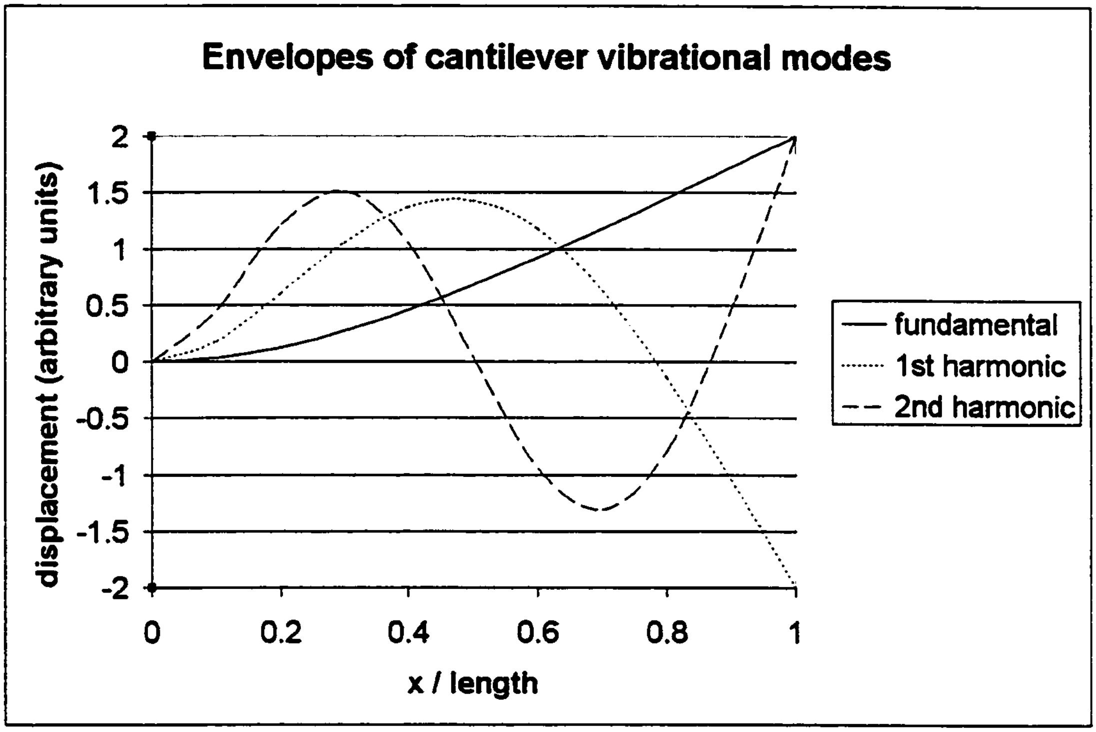

Figure 2.1. Cantilever vibrational modes. The first three modes of fixed-free beam vibration are shown as a function of position along the length of the beam. The lower the order of the harmonic, the more that deflection is constrained towards the tip of the beam. The fundamental may therefore be the mode of choice for small-volume viscometric application.

Viscous effects are not the only forces contributing to a measurement of "shear force"; van Der Waals and larger scale electromagnetic forces may contribute to a significant degree (cf. Israelachvili and Tabor, 1972; Xu and Yeung, 1998). It would therefore be advantageous to have an independent, preferably non-mechanical, measure of probe-sample distance, so that such distance-dependent factors could be accounted for or avoided.

Considerable effort in our lab has been put into the development of an all-optical probe-sample distance control scheme, based on laser feedback. When light from a laser is reflected back into the lasing cavity, the amplitude and frequency of the lasing are perturbed. As little as -80 dB of reintroduced light can produce a clearly measurable effect, while the interferometric nature of the technique can allow monitoring of the position of the reflector with near-atomic precision (Tkach and Chraplyvy, 1986; O'Neill and Bearden, 1995).

The potential sensitivity of this technique makes it an attractive candidate for the basis of an optical probe-sample distance control scheme. To date, however, this method has not reached adequate fruition for use completely independent of shear-force feedback. It was decided to concurrently explore steady-state fluorescence anisotropy as an inexpensive, more immediately implementable alternative for small-scale viscometry.

2.4 Fluorescence anisotropy

In a Steady-State Fluorescence Anisotropy (SSFA) measurement, a solution of a macromolecule tagged with a fluorophore is excited with polarized light. The excited macromolecule-fluorophore conjugates will experience Brownian motion during the fluorescence lifetime of the fluorophore, after which a photon will be emitted polarized parallel to the respective emission dipole of each fluorophore. Excitation and detection are continuous, resulting in a temporally averaged signal. A cartoon of such a measurement is given in **Figure 2.2**.

The resulting fluorescence is separated by a polarizing beamsplitter into its two component polarizations, F_{par}, the fluorescence polarized parallel to the excitation light, and F_{prp}, the fluorescence polarized perpendicular to the excitation. The fluorescence anisotropy, r, is defined by the equation

$$r = (F_{par} - F_{prp}) / (F_{par} + 2 F_{prp}),$$

representing the intensity difference between the measured channels, normalized by the total amount of fluorescence. (The factor of 2 appearing with F_{prp} in the denominator serves to account for fluorescence emitted with a polarization paraxial with the direction of incidence of the excitation light in addition to the cross-polarized fluorescence).

The apparent value of r in the limiting case of the direct incidence of the fully polarized excitation light upon the detectors ($F_{prp} = 0$), would thus be 1. In the case of a population of randomly oriented fluorescing molecules, there will be preferential excitation of fluorophores with dipoles aligned with the excitation polarization; still, the polarization of the emission will be less than total. An r of at most 0.4 is attainable, given completely immobile fluorophores (See the **Appendix** for a derivation of this result).

Given knowledge of the fluorophore's fluorescence lifetime, the degree to which the fluorophore is free to rotate may be then determined using the relation

$$r = r_0 (\phi / (\phi + \tau_f))$$

Fluorescence Anisotropy: Principle

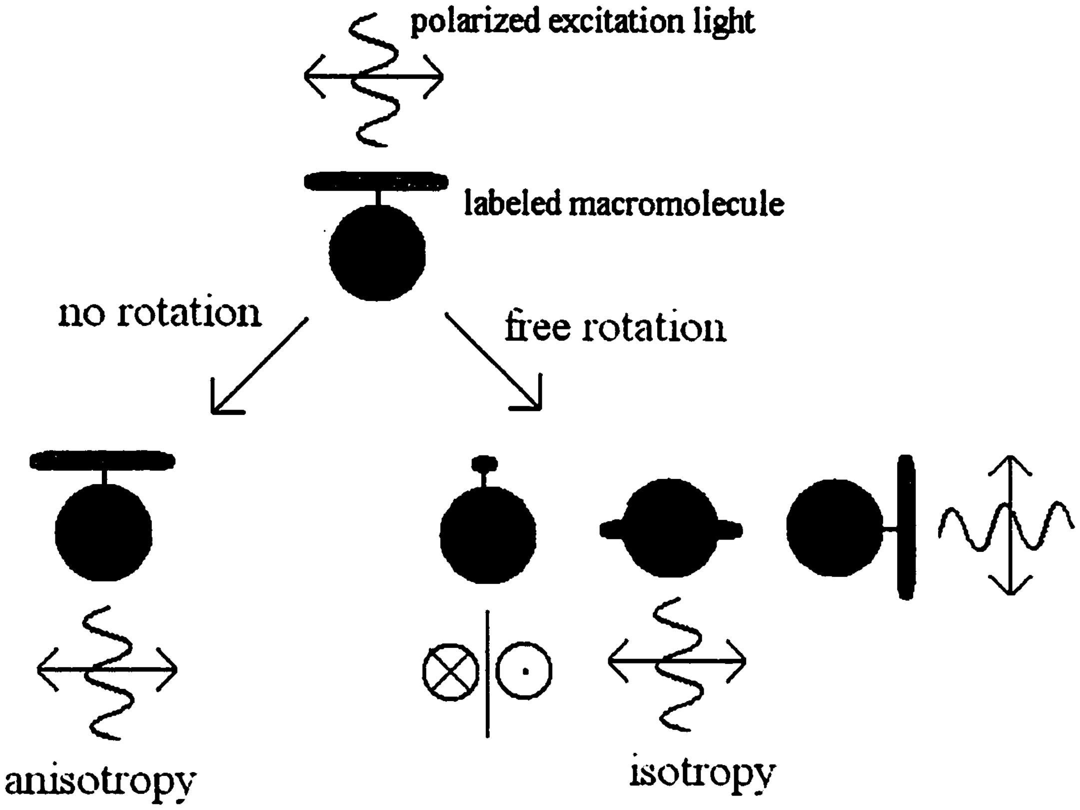

Figure 2.2. Fluorescence anisotropy. In a fluorescence anisotropy measurement, a fluorophore attached to and/or within a macromolecule is excited by polarized light. During the finite lifetime of the excited state of the fluorophore, the macromolecule undergoes some degree of rotational diffusion. The resulting degree of fluorescence polarization provides a measure of this rotational freedom, and therefore of microviscosity.

where r_0 is the anisotropy in the absence of rotational freedom, τ_f is the fluorescence lifetime of the fluorophore and ϕ is the rotational correlation time of the fluorophore. ϕ is in turn related to the rotational diffusion coefficient by the relation

$$\phi = 1 / (6 D_r).$$

The rotational diffusion coefficient, D_r, is given by

$$D_r = k T / (8 \pi \eta R_h^3)$$

where k is the Boltzmann constant, T is temperature, η is viscosity and R_h is the hydrodynamic radius of the species in question.

Given knowledge of the hydrodynamic radius of the labeled macromolecule in question, it is therefore possible to extract viscosity information from a measurement of fluorescence anisotropy.

The "viscosity" measurement thus provided, however, is distinct from a measure of bulk viscosity, in that only the immediate environment of the macromolecule is sampled. Rotationally determined viscosities are thus termed *microviscosities.*

2.5 Microviscosity

Solutions can be viscous for different reasons. Large polymers can, by virtue of their bulk, inflexibility, and/or tenuousness, induce a high macroscopic viscosity (Witten, 1990). The microviscosity experienced by a solute within a small domain of solvent between such polymer strands, however, might be significantly less than this value, depending upon the relative size of the polymer "co-solvent". Lavalette et al. (1999) quantified this phenomenon, producing the relation

$$\mu = \eta_{solvent} \times (\eta_{solution} / \eta_{solvent})^{Q},$$

where μ is the microviscosity experienced by a diffusing solute, $\eta_{solvent}$ is the viscosity of the primary solvent, $\eta_{solution}$ is the solvent macroviscosity, and

$$Q = (1 + M / 8800)^{(-15.3 / R)},$$

where M is the co-solvent mass in daltons, R is the diffusing solute's hydrodynamic radius in angstroms.

Steady state fluorescence anisotropy can provide a measure of microviscosity, which may provide clues to small-scale solvent behavior, but can the technique be scaled down to sub-micron scales?

2.6 Fluorescence Anisotropy NSOM (FANSOM) feasibility

2.6.1 NSOM probe polarization retention

Fluorescence anisotropy as a technique requires that the illuminating light be polarized. Frequently, probes will have imperfections that randomize polarization. It is not uncommon, however, for probes to exhibit > 90% polarization, and several forms of polarized light NSOM are precedented, including polarization microscopy and phase modulated polarimetry (Betzig et al., 1992b; von Freymann et al., 1999; Shin et al., 1999; McDaniel et al., 1998).

Given a completely immobile fluorophore excited by incompletely polarized light, it can be shown that

$$F_{par} = 0.6 \times (I_{par} + I_{prp} \times 2/3) / (I_{par} + 2\, I_{prp})$$

and

$$F_{prp} = 0.2 \times (I_{par} + 4\, I_{prp}) / (I_{par} + 2\, I_{prp})$$

where I_{par} and I_{prp} are the intensities of the polarization components of the excitation light parallel to and perpendicular to the direction of maximum polarization (see the **Appendix** for a derivation of these relations).

These values lead to a value of the anisotropy in the absence of rotational freedom, r_0, of somewhat less than 0.4, resulting in a system sensitivity correspondingly reduced from ideality.

The non-zero NA of the detection optics will also induce overlap in what would otherwise be orthogonal channels, as given by the relations

$$F_{par} = K_a\, F_x + K_b\, F_y + K_c\, F_z$$

and

$$F_{prp} = K_a\, F_x + K_c\, F_y + K_b\, F_z,$$

where

$$K_a = (1 / 6) (2 - 3 \cos \sigma + \cos^3 \sigma) / (1 - \cos \sigma),$$

$$K_b = (1/24)(1 - 3\cos\sigma + 3\cos^2\sigma - \cos^3\sigma)/(1 - \cos\sigma),$$

$$K_c = (1/8)(5 - 3\cos\sigma - \cos^2\sigma - \cos^3\sigma)/(1 - \cos\sigma),$$

F_x, F_y, and F_z are the directional components of the polarization of the fluorescence, and σ is the half angle defined by the NA of the objective used (Axelrod, 1989; Yoshida and Asakura, 1974). In the case of the objective used in the system described herein, a Leitz 32×, 0.6 NA infinity-corrected objective, this effect is expected to result in a reduction of r_0 from 0.4 to 0.375.

2.6.2 Light levels

Assuming adequate polarization, will the modest amount of fluorescence available be enough to produce a usable signal?

The light intensity is limited by the probe tip to ~ mW incident from within the optical fiber. Most of this light is absorbed by the tip, causing heating, which in turn melts the aluminum coating off of the probe, widening the aperture.

A typical etched, as opposed to pulled, probe has a transmission of ~ 1/1000, yielding 1 µW of excitation light (Bukofsky and Grober, 1997). The amount of this light transformed into fluorescence depends logarithmically upon the absorbance A of the excited solution, as given by the equation

$$A = \varepsilon BC,$$

where C is the fluorophore concentration, ε is the extinction coefficient of the fluorophore and B is the distance of fluorophore solution traversed. For a near-saturated solution of a typical, commercially available fluorescein-labeled dextran, C ~ 3 mM and $\varepsilon = 78{,}000\ \mathrm{mol^{-1}\ cm^{-1}}$. Assuming a generous, and yet still near-field B of 100 nm, A = 0.00234, or ~ 0.5% of photons absorbed. Of the aforementioned 1 µW of excitation, this represents ~ 5 nW.

An efficient and high NA objective can theoretically collect one half-sphere of this fluorescence, or ~ 2.5 nW, a value easily within the range of a PMT detection scheme.

It looked possible on paper, but would it really work?

3. The FANSOM system

3.1 System overview

The system was built around an Axiovert 100TV base, as schematized in **Figure 3.1**. The subparts of the system are described below.

3.2 Light source and conditioning

The light source is a 50-mW argon-ion laser (Ion Laser Technology, Salt Lake City, Utah). The laser was adjusted for operation at 488 nm to coincide with the absorption peak of fluorescein. Due to a quirk of the laser's control electronics, the small amount of 60 Hz noise evident in the laser output was found empirically to be minimized by setting the laser to a mid-range power of ~ 20 mW (resulting in a 10-fold noise reduction relative to threshold operation!). The laser was left set at this output power, and all necessary control of the power reaching the probe was achieved with neutral density filters and/or a crossed polarizer placed between the laser and the last polarizer.

Percent degree of polarization (% D.O.P.) is given by

$$\% \text{ D.O.P.} = (I_{par} - I_{prp}) / (I_{par} + I_{prp}),$$

where I_{par} and I_{prp} represent the intensities of the polarization components parallel and perpendicular to the direction of maximum polarization, respectively. The emission from the laser was found to be ~ 95% polarized, improving to ~ 99% with the addition of the aforementioned external polarizer.

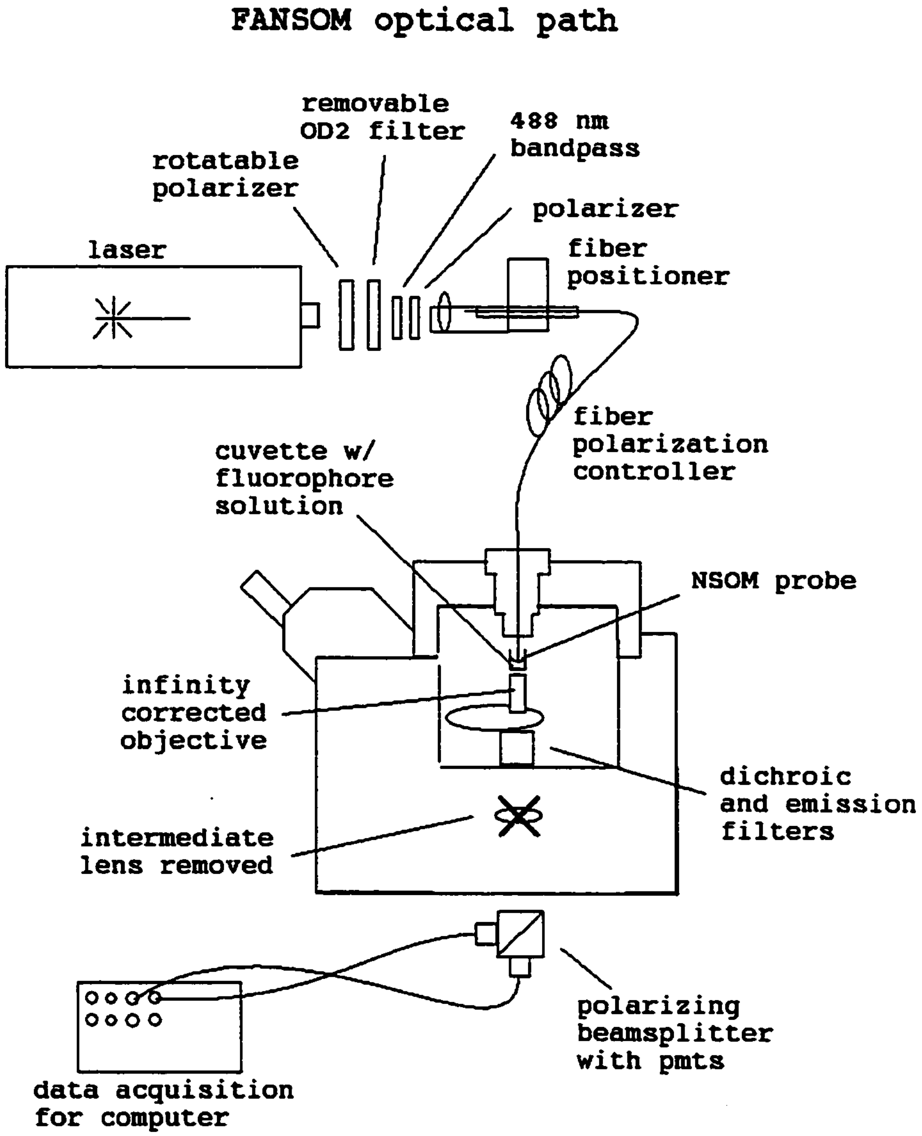

Figure 3.1. FANSOM optical path. In the current FANSOM implementation, polarized light from a laser is launched into an optical fiber, which is strained as necessary to maintain linearity of the polarization at the NSOM probe end of the fiber. A cuvette containing a solution of macromolecules calculated to have ~ 1 mM of attached fluorescein, in addition to buffer components as dictated by the sample to be investigated, is raster scanned under the NSOM probe. The resulting fluorescence is collimated by an infinity-corrected objective lens, separated from the excitation light by standard dichroic and emission thin-film filters, and analyzed by a polarizing beamsplitter. The two resulting channels of fluorescence are measured by photomultiplier tubes and digitized for recording and analysis.

A narrow bandpass thin-film filter (488NB3) was used to be certain that no other lasing modes or emissions would be admitted to the probe.

All such free-space elements placed between the laser and NSOM probe fiber optic were placed at a slight angle (~ 3°) relative to the beam axis to avoid laser noise due to optical feedback (found for this laser to be ~ 1% anode current change per 5% reflectance at low reflectances; data not shown). The fiber of the free-space-to-fiber coupler was spliced to a fiber that conveyed the light to the optical table, which in turn was spliced to the fiber of the NSOM probe tip.

Bends in the lengths of optical fiber introduce strain birefringence, which circularizes the polarization of light propagating in the fiber. An equal and opposite amount of birefringence was introduced by including controlled bends in the central length of fiber with a three-paddle fiber polarization controller to re-linearize the polarization of the light exiting the probe (Thorlabs, Inc., Newton, NJ). The retardance R of a loop (full or partial) of optical fiber is given by

$$R = k\,n\,/\,(D\,\lambda),$$

where n is the number of loops in the bend, D is the diameter of the loops, λ is the wavelength of propagating light, and k is an empirical factor; in the case of the Newport F-SA, 488/514 single-mode fiber used, $k = 39{,}400\ \mu m^2$ radians.

By winding the appropriate number of loops around a paddle of the fiber polarization controller such that one quarter wave of retardance is obtained, an effective "quarter wave plate" can be constructed. Thereafter, simple rotation of the paddle allows linearization of the polarization exiting the NSOM probe tip.

Similarly, a half wave plate may be constructed using another paddle of the controller, allowing arbitrary rotation of the linearized polarization.

3.3 Nanopositioning

The nanoposition systems used are schematized in **Figure 3.2**.

Vertical probe positioning with 2-nm precision over a range of ~ 2.5 cm was achieved using a Burleigh ARIS 11 Inchworm with ARIS 950/ULN controller (Burleigh Instruments, Inc., Fishers, NY). Vertical motions were performed with an attached quadrant piezoelectric tube controlled over its +/- 3.5-um range by a 16-bit D/A signal, corresponding to a precision of ~ 0.1 nm.

The sample was laterally positioned by stage micrometers for coarse positioning and a Queensgate NPS-XY-100A X-Y stage/NPS3330 controller (Queensgate Instruments, Inc., East Meadow, NY) for fine (1-nm accuracy) control over a +/- 50-μm range.

3.4 Probe manufacture

NSOM probe tip tapers were formed by "tube-etching", wherein optical fibers are simply left dipped, plastic buffers intact, into ~ 50% HF (Stockle et al., 1999; Lambelet et al., 1998a). A probe shaped by this method and then coated is shown in **Figure 3.3**. As the glass core and cladding react with the HF and solvate, the local solution density increases. The denser solution sinks, allowing in fresh HF, forming a quasi-convection cycle within the buffer. The result, after ~ 90 minutes, is a highly even, smooth taper. The buffer is removed from around the taper by softening in

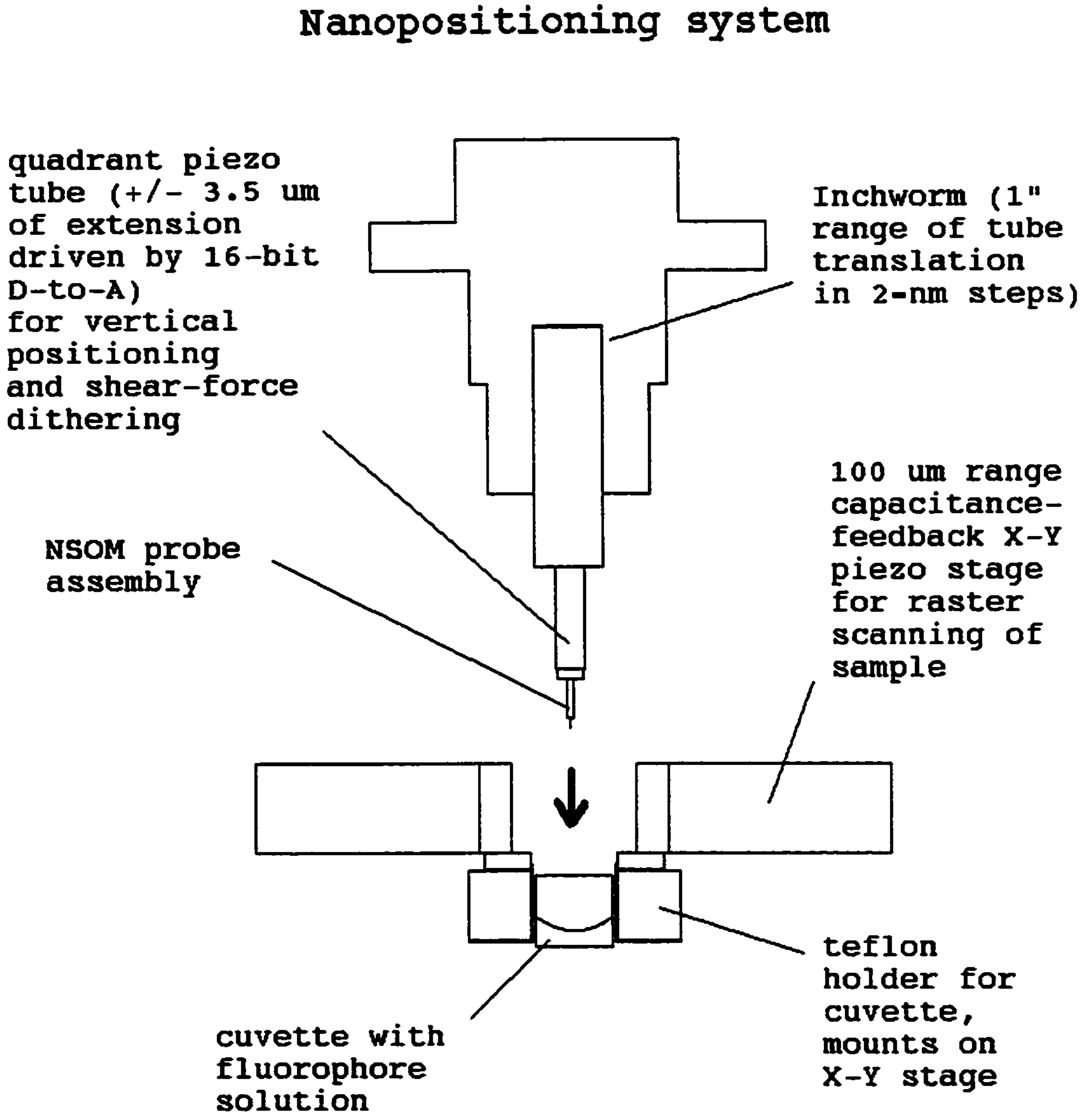

Figure 3.2. Nanopositioning system. The NSOM probe is positioned vertically by a quadrant piezo tube with ~ 0.1-nm precision, which in turn is positioned over a range of ~ 1" by a Burleigh Inchworm (Burleigh Instruments, Inc., Fishers, NY). The sample is scanned under the probe with 1-nm accuracy by a capacitance-feedback piezoelectric X-Y stage (Queensgate Instruments, Inc., East Meadow, NY).

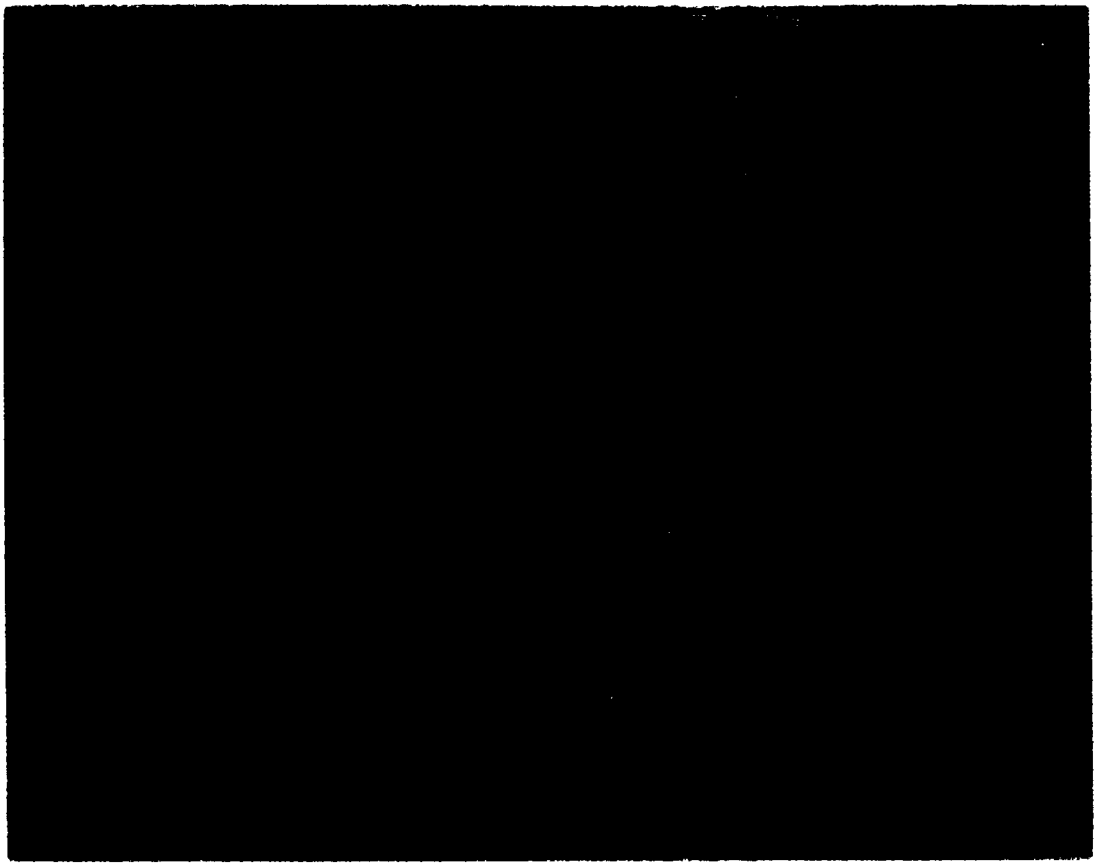

Figure 3.3. SEM of an etched NSOM probe. Optical fibers are tapered to a tip with a radius of curvature of tens of nm by acid etching within their plastic buffer. The resulting tapers are evaporatively coated with a thin (~ 1-nm) layer of chromium and a subsequent, thicker (~ 50-nm) layer of aluminum. The chromium promotes adhesion of the aluminum, minimizing heating damage and detachment of the aluminum when submerged for prolonged periods, while the aluminum provides superior opacity. The sharper tips of etched relative to pulled probes make their apertures invisible to SEM examination.

concentrated H_2SO_4 for 30 minutes, after which the buffer sloughs off, either by itself or with gentle coaxing with fine tweezers. The key advantage of etching as opposed to the heat-drawing of probes is that the core remains unnarrowed nearly all the way to the tip. Given the exponential nature of light attenuation by sub-wavelength waveguides, a large efficiency improvement is realizable (transmission of ~ 0.1% vs. ~ 0.0001%; Bukofsky and Grober, 1997). Another advantage is the avoidance of strain birefringence induced in the pulling process (von Freymann et al., 1999).

The probes are then coated with an adhesion layer of ~ 5 nm of chromium, followed by ~ 50 nm of aluminum. Aluminum is chosen for its low skin depth (7.1 nm; Bruijn et al., 1992) and correspondingly high absorption given a minimum of thickness, but it can detach from the glass substrate when subjected to solutions for prolonged periods (~ 1 hour). The chromium layer improves adhesion, and no such problems have been noted since the implementation of its use (cf. Stockle et al., 1999). The coating angle, source-target distance, and rates of coating were designed to coincide with those of Stockle et al. (1999).

Note that while the break that terminates heat pulling results in an end facet which is visible to a scanning electron microscope, etching leaves a tip too sharp to resolve (Lambelet et al. 1998a).

Probes were mounted into steel collet/capillary assemblies for magnetic mounting to the quadrant piezo tube of the nanopositioning system. Super-glue gel was found necessary to ensure a sound mechanical coupling between the tube and collet. The glue was removed with acetone as necessary for probe exchange.

A jig was designed for micrometer control and microscopic measurement of the positioning of the fiber within the colleted capillary during gluing, allowing the cantilevered extension of the fiber to be set with ~ 50-µm precision (cf. Barenz et al.,

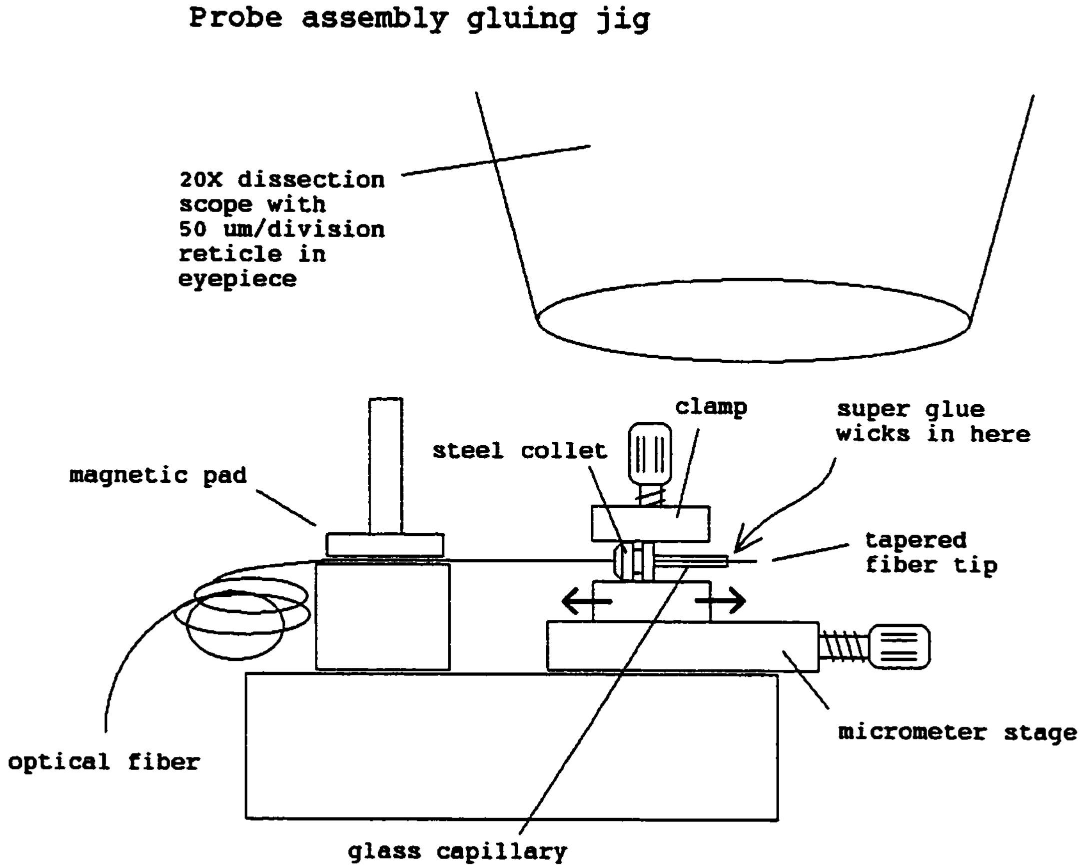

Probe assembly gluing jig

Figure 3.4. Probe assembly gluing jig. By microscopic observation and control of the NSOM probe tip relative to the collet and capillary that serve to mount the tip to the rest of the system, the protruding length of optical fiber may be controlled to within ~ 50 microns. With this precision, the resonant frequency of the cantilevered fiber may be reproducibly chosen with ~10% error. The frequency at which the shear-force subsystem operates may thus be selected to avoid undesirable resonance with other mechanical parts of the system.

1996). This jig and the resulting probe assembly are shown in **Figure 3.4**. A non-gel super glue was found to have preferable wicking characteristics for this step in the probe manufacture process. Given precise control of tip length, the resonant frequency of the tip can be predetermined to within ~ 10%, facilitating the discrimination of fundamental, lateral tip resonances from other vibrational modes and spurious system resonances. Example spectra, as measured by the shear force system described below, are shown in **Figure 3.5**. In air, peaks are visible at ~ 13 kHz and ~ 24 kHz, corresponding to a resonance of the piezo tube itself and the vibration of the NSOM probe tip. With the probe tip underwater, the probe vibration is damped, decreasing the Q of the probe resonance, and the resonance is lowered in frequency; the ~ 24 kHz peak is shifted to ~ 20 kHz.

Though strategies involving the minimization of solution depth have been developed to counter this damping, applications of the shear force system to date have not been critical enough to necessitate such measures (Gheber et al., 1998; Lambelet et al., 1998b).

3.5 Shear force system

The shear force system used for probe-substrate distance determination is shown in **Figure 3.6**. A small (~ 10 nm p-p) vibration perpendicular to the plane of the figure is imposed on the quadrant piezo tube at the reference frequency of the lock-in amplifier. The frequency of this vibration is selected to coincide with the fundamental lateral resonance of the NSOM probe tip.

Light of 635-nm wavelength from a laser diode is focused upon the tip, brightly illuminating it. A collecting lens is used to form a somewhat magnified (~ 3×) real

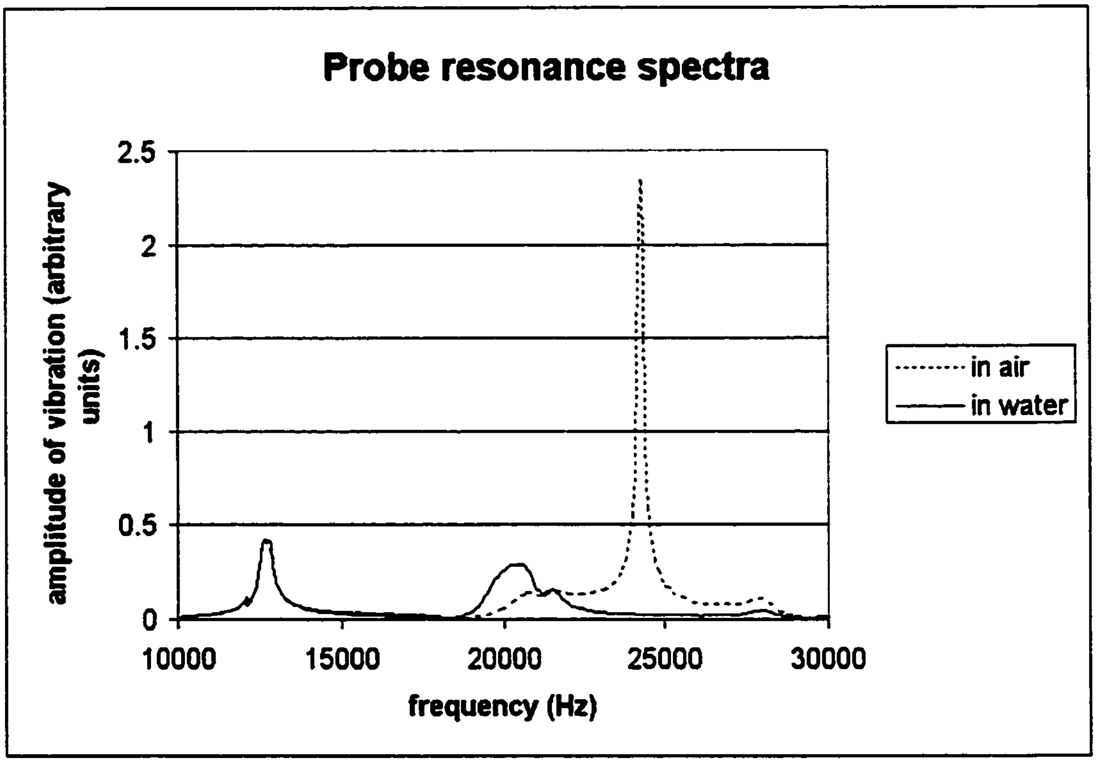

Figure 3.5. Probe resonance spectra in air and water. The vibrational spectra of a representative cantilevered NSOM probe in air and in water are shown. The Q of the probe resonance is reduced in the more highly damping water environment relative to that of air, concurrent with a drop in resonant frequency (from ~ 24 kHz in air to ~ 20 kHz in water). The peak common to both spectra at ~ 13 kHz is that of the driving piezo tube, situated in air above the cuvette in both cases.

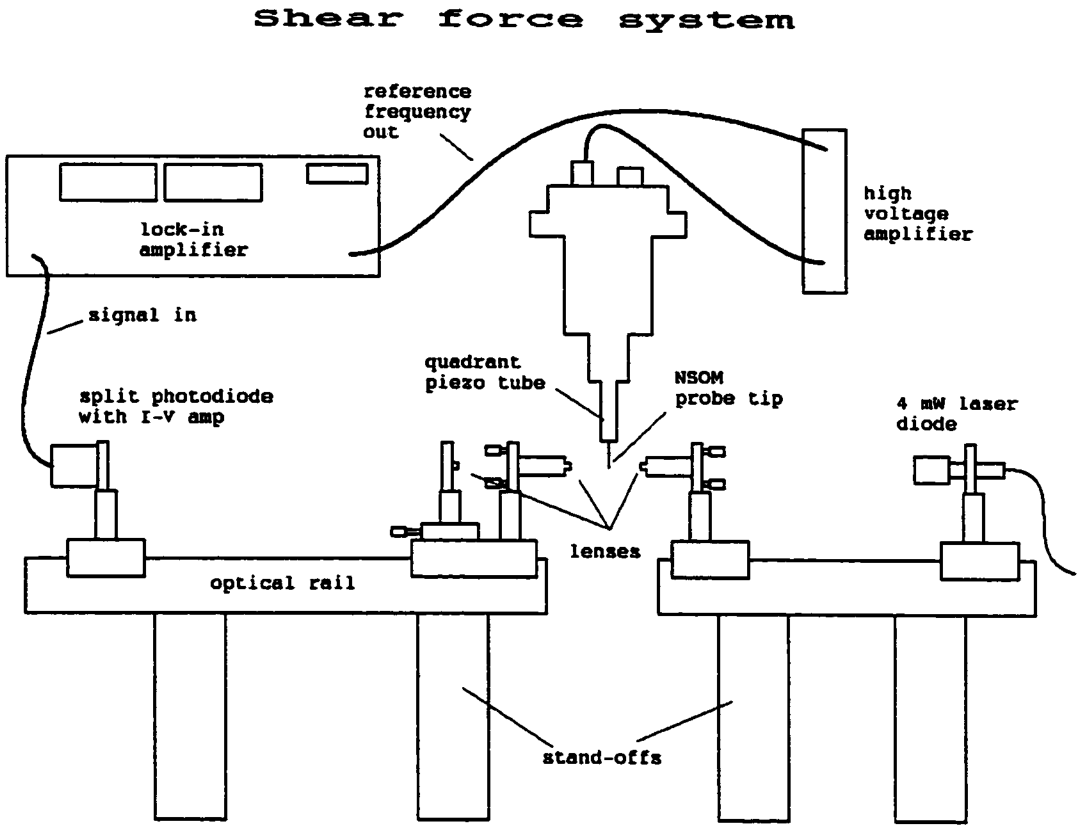

Figure 3.6. Shear-force system. In the shear force system as implemented herein, the reference frequency of a lock-in amplifier is selected to coincide with the fundamental probe resonance and used to drive probe vibration (~ 5 - 50 nm p-p) via the quadrant piezo tube. A magnified shadow of the vibrating tip is projected upon a split photodiode, and the resulting signal is monitored by the lock-in amplifier.

image of the resulting shadowed profile of the probe. The image is then further magnified to ~ 100× in its subsequent projection onto a split photodiode. This two-stage magnification scheme allows for the long working distance necessary to image the probe from outside of the sample cuvette, while keeping the whole of the apparatus compact enough to fit on the optical table.

The resulting differential signal from the split photodiode is returned to the lock-in amplifier for filtering. Lock-in detection takes advantage of the trigonometric identity

$$\cos(f_1)\cos(f_2) = 0.5\cos(f_1 - f_2) + 0.5\cos(f_1 + f_2)$$

to extract periodic signals from background noise. In a lock-in scheme, the phenomenon of interest and measurement thereof are both modulated at a set frequency f. Sum and difference frequencies ($2f$ and 0 Hz) result from demodulation of the measured signal. As the DC component at this point reflects the amplitude of the signal present at frequency f, it is possible to reject the majority of extraneous frequency content simply by low pass filtering.

As the probe tip approaches to within tens of nanometers from a surface, tip-surface interactions serve to dampen the resonance of the probe, resulting in a drop in measured shear force signal. An approach curve is shown in **Figure 3.7**. Typically the amplitude of the measured vibration is used to determine distance from the surface in question, though as suggested by the figure, phase information can also be used (Barenz et al., 1996). Some piezo tube hysteresis is evident, resulting in an apparent lengthening of the retracting shear force curve.

The precise location of the surface is generally considered to correspond to the minimum measured shear signal, though in practice, this minimum is not known with

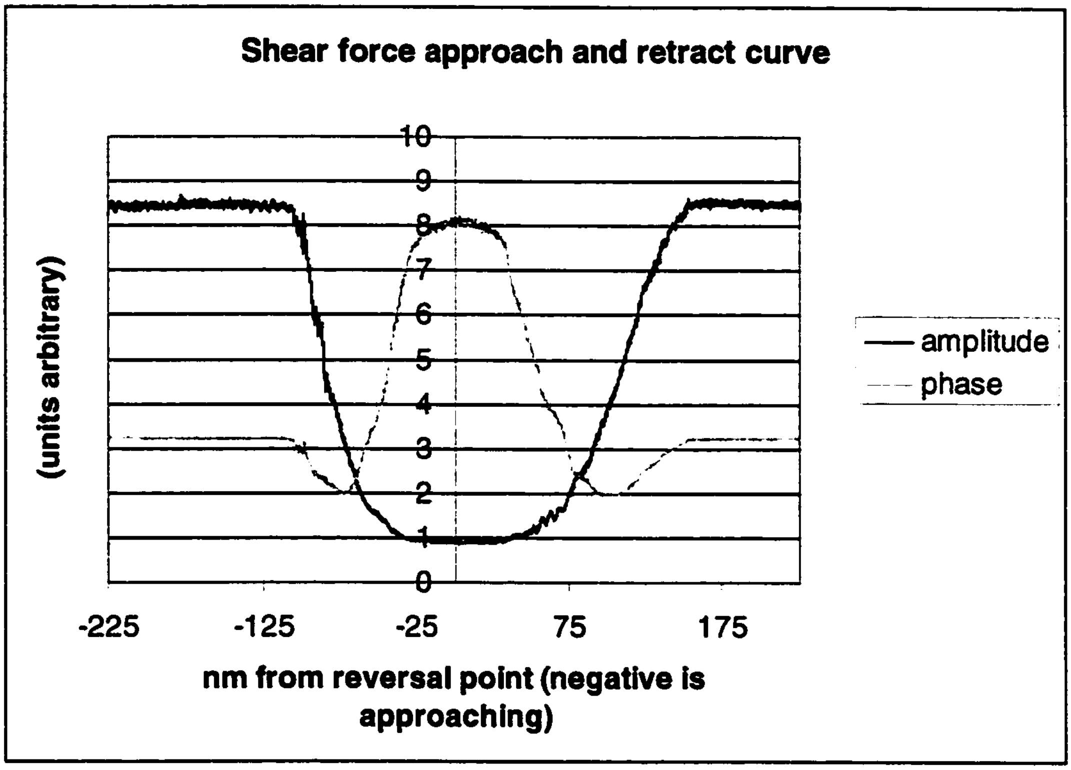

Figure 3.7. Shear-force approach curve. As the vibrating NSOM probe nears the surface to within tens of nm, the probe resonance is perturbed, providing a measure of probe-sample distance. The amplitude of the lock-in signal of the shear force system drops to a minimum, which is commonly taken to indicate contact with the surface. In the curve shown, hysteresis in the piezo tube used to extend and retract the probe produces an apparent elongation of the retraction curve. The signal to noise ratio is high, allowing ~ nm changes in probe-sample distance to be discerned.

certainty until the surface is contacted. The full range of the approach curve depends upon the probe and surface used, and the medium in which the approach is performed, though ~ 30 nm is typical (Durkan and Shvets, 1996; Okajima and Hirotsu, 1997). Surface localization to within less than ~ 10 nm is therefore possible.

3.6 Polarized photodetection

The rejection of background fluorescence is a key design goal for a FANSOM system. The presence of fluorophore in the bulk solutions used, combined with the short absorbance pathlength between the probe and substrate, calls for several measures in separating emission light from excitation. An angled dichroic filter chosen for fluorescein excitation and emission (OD_{488} ~ 2) was included in the collection path, and black felt was used to intercept excitation light refleted from this filter. This arrangement served to discard the excitation light, which would otherwise reflect off of the subsequent high-Q emission filter (OD_{488} ~ 3) and confocally excite the fluorophore bath around the NSOM tip. The use of a second emission filter proved of little added benefit, as the effectiveness of thin-film filters is highly reduced by multiple reflections between parallel filters.

A polarizing beam splitter was placed below the lower camera port of the Axiovert 100TV base as shown in **Figure 3.1** to separate the polarization components of the collected fluorescence. It is critical to the operation of such beam splitters that incoming light be incident very close to normal to the cube face (within ~ 3°). This condition was achieved by removing the intermediate lens from the Axiovert base, allowing the essentially collimated, infinity-corrected optical light path to be directly incident on the cube. Small PMTs (Hamamatsu R5600U) were secured directly to the side and bottom of the polarizing beamsplitter cube.

Before each experiment, the differing sensitivities of the two PMT channels were determined by a method adapted from Axelrod, 1989. The inchworm/probe assembly was removed from the microscope and a penlight, diffused by two Kimwipes rubberbanded over its end, was shone down into the microscope from varying distances. The outputs of the upper and lower PMTs were converted into an X-Y plot. The slope of the best fit line was taken as the ratio G between the channel sensitivities, and used to correct calculations of SSFA and % D.O.P.

In later experiments a small, non-zero Y-intercept was noted in the PMT sensitivity X-Y plot. This offset was likely due to the introduction of the angled dichroic filter, which can serve to polarize transmitted light. The best fit line including this offset was then used to transform obtained data.

To minimize noise sources, the bandwidth of the system was adjusted to match that of the rate-limiting factor. The Labview software used to collect data limited the data sampling rate to ~ 25 Hz, or one point every ~ 40 ms. This value specified several other system parameters, as follows:

As a rule of thumb, for lock-in detection of a signal to be sampled, it is best to allow the amplifier to settle to each new value for at least five times the RC time constant τ of its low-pass filter,

$$\tau = 1 / (2 \pi f_0),$$

where f_0 is the pole frequency of the low pass filter. Given the above rate of 40 ms per sample, a τ of at most 8 ms is desired. The lock-in's filter should be set with its pole at least one decade below the sum frequency $2f$ to be rejected; this condition suggests operation with a reference frequency of ~ 100 Hz. (A value of 95 Hz was chosen so as to maximize the least common multiple of the drive frequency and 60

Hz, the most likely source of aliasing). The current-to-voltage converters supplying the raw signal to the lock-in were modified to limit their bandwidth to ~ 290 Hz, or ~ 0.5 decades beyond the frequency of modulation.

The resulting signals were digitized by a PCI-MIO-16XE-10 data acquisition card (National Instruments, Austin, TX) under control by Labview software (ibid.).

Buffers of up to 1000 data points per input channel were acquired at 100 kHz and held until averaged and displayed by the data acquisition software.

3.7 Confocal operation

Another measure used to reject background fluorescence, in addition to use of conventional interference filters, was modification of the microscope for confocal operation. This modification was used in later experiments requiring long vertical scans through the plane of focus. Two aspheric lenses were arranged confocally with respect to each other with a pinhole at their focus, as shown in **Figure 3.8**. This assembly was inserted in place of the intermediate lens, further rejecting light not originating from the point of objective lens focus, and therefore rejecting rays of light not precisely parallel to the infinity-corrected light path.

A good compromise between light collection efficiency and background rejection, recommended by Leica for typical microscope geometries, is to use a pinhole diameter D such that

$$D = M\, 3.8\, \lambda / (2\, \pi\, NA),$$

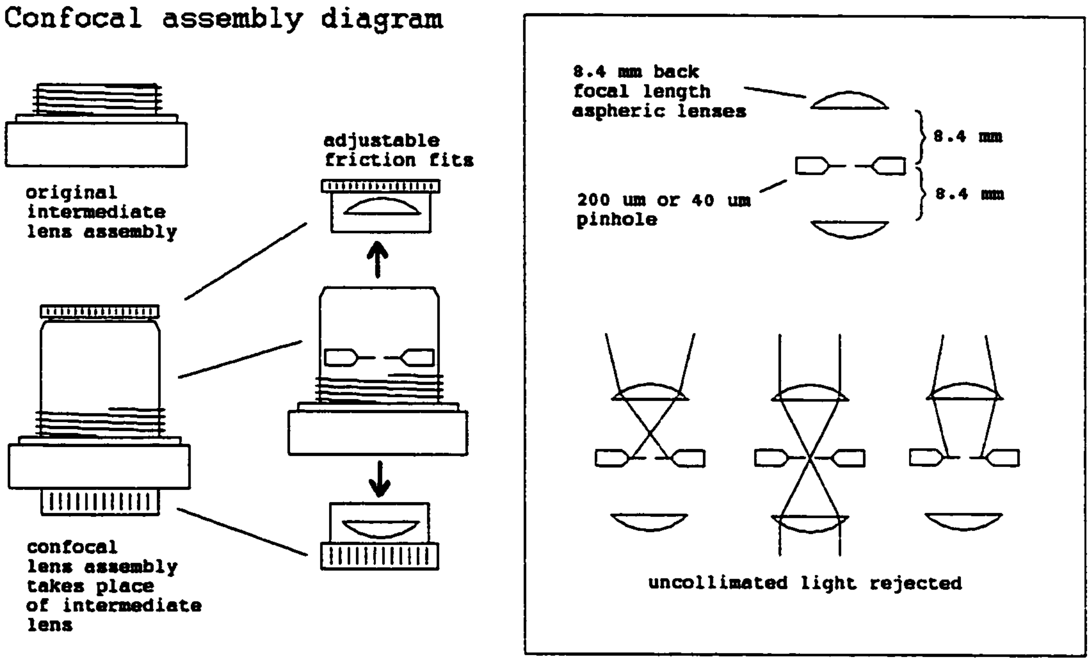

Figure 3.8. Diagram of confocal assembly. In some experiments, to reject background fluorescence and to avoid the incidence of uncollimated light upon the polarizing beamsplitter, a confocal assembly was introduced in lieu of the previously removed intermediate lens. The assembly's aspheric lenses are arranged confocally, with a pinhole at their focus, so as to pass only collimated light, and thus, preferentially, light originating from the NSOM probe at the focus of the infinity-corrected objective.

where M is the total magnification of the system between the specimen and the pinhole, λ is the primary wavelength of light used, and NA is the numerical aperture of the chosen objective. The factor of 3.8 is empirical, roughly indicating the desired aperture size to the diameter of the Airy disc characteristic of the microscope.

For the FANSOM system as constructed, this factor would correspond to a pinhole size of 16 μm. However, following the lead of Haydon et al., 1996 in which a pinhole was used for an NSOM system geometry, a larger pinhole (~ 200 μm) was initially used.

To evaluate the efficacy of the modification, the probe tip was extended through the plane of focus while the amount and degree of polarization of the collected light was monitored. Such focus-through data is shown in **Figure 3.9**.

The focus-through in the absence of a pinhole, **Figure 3.9a**, shows variation from two main sources:

(1) The polarizing beamsplitter cube used to separate the orthogonal polarizations is designed for use only with light with incidence normal to the surface. In the case of the infinity-corrected optics used, with no intermediate lens, only light coming from the plane of focus will meet this criterion. When the probe is moved above and below this point, the light incident on the cube will be converging, or diverging, respectively, resulting in compromised cross-extinction.

(2) The photocathodes of the PMTs used are gridlike, containing light-insensitive lines separating fields of photosensitive area. When the probe is significantly above the plane of focus, a conjugate image plane can be made to coincide with the PMT surface, which may result in an undesirable concentration of light between photosensitive fields.

(a) Effect of focus before 200 um confocal pinhole

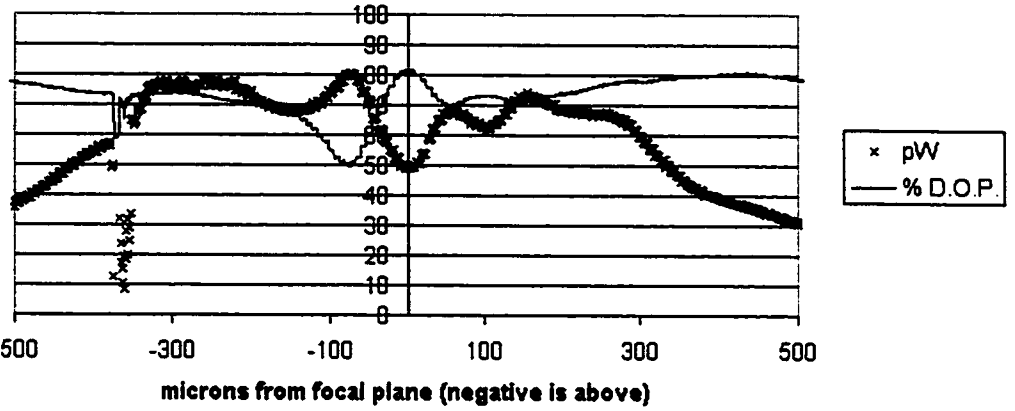

(b) Effect of focus with 200 um confocal pinhole

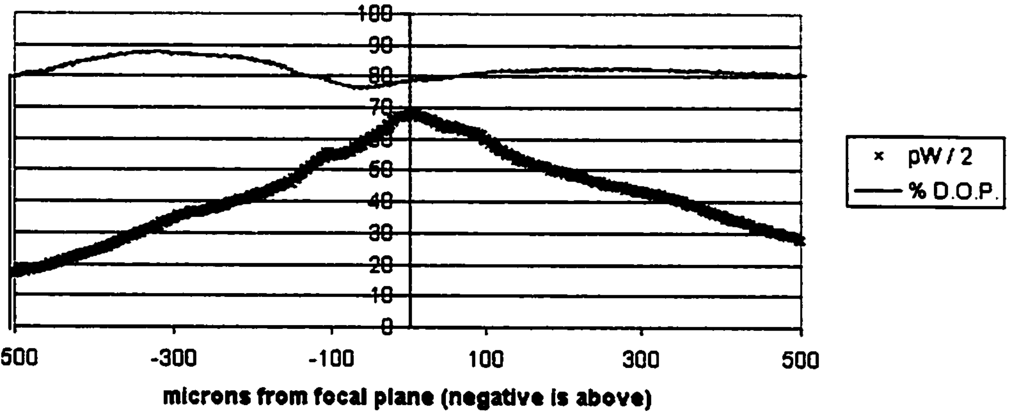

Figure 3.9. Effect of defocusing on collected light with 200-micron pinhole. In the absence of the confocal assembly (a), uncollimated light reaches the polarizing beamsplitter, resulting in channel crosstalk and uneven illumination of the spatially varying surface of the PMT cathodes, appearing as variation in measured degree of polarization (% D.O.P.) and total light intensity (shown in pW). With the assembly in place (b), the sensitivity of the polarization to misadjustment of focus is much reduced, and the total light intensity becomes simply linear with distance from ideal focus. Also, the FWHM of the total light intensity curve is reduced by 30%, providing improved vertical system resolution.

Figure 3.9b shows a focus-through of the same probe with the confocal insert in place, using a 200-μm pinhole. Both variation sources are diminished; the sensitivity of the apparent degree of polarization to the distance out of focus has dropped from ~ 1% per 2 microns to ~ 1% per 35 microns, and the light level fluctuations are essentially absent. Also, the FWHM of the peak is reduced by ~ 30%. The peak light collection was reduced by ~ 2% +/- 5% by the inclusion of the pinhole.

The same experiment was later conducted with a 40-μm pinhole, closer in size to the theoretical ideal; the results are shown in **Figure 3.10**.

A new probe was used, and the baseline in the absence of the confocal insert was again measured (**Figure 3.10a**). Variations similar to those of the previous experiment are found. **Figure 3.10b** shows results are similar to that of the case of the 200-μm pinhole, with a FWHM reduction of ~ 70% relative to the no-pinhole case. The peak intensity, however, was found to be reduced ~ 70-fold.

This disadvantage, in combination with an increased difficulty in making manual adjustments due to reduced visibility through the microscope oculars, caused us to prefer the use of the 200-μm pinhole for subsequent experiments.

3.8 Fluorophore development and choice

Fluorescence anisotropy, as a measurement technique, depends critically upon the choice of fluorophore, the macromolecule it is attached to, and the rigidity of their connection. What is the optimal probe for the FANSOM system at hand?

Fluorescein was initially chosen as the fluorophore of choice due to the close match of its absorption spectrum with our pre-existing laser, and because of the precedent of its

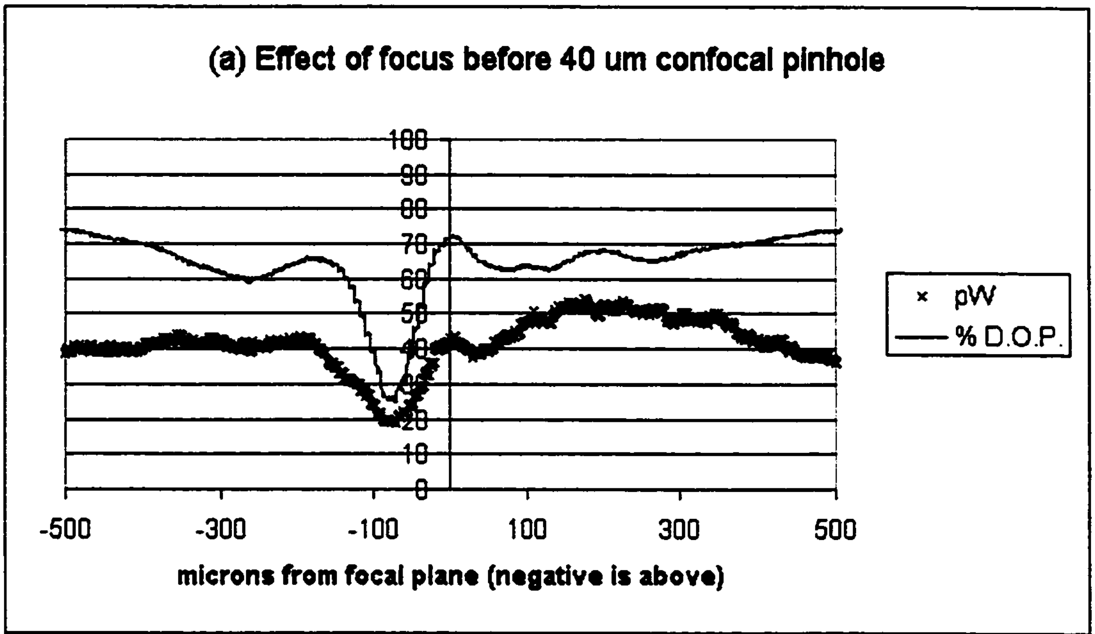

(a) Effect of focus before 40 um confocal pinhole

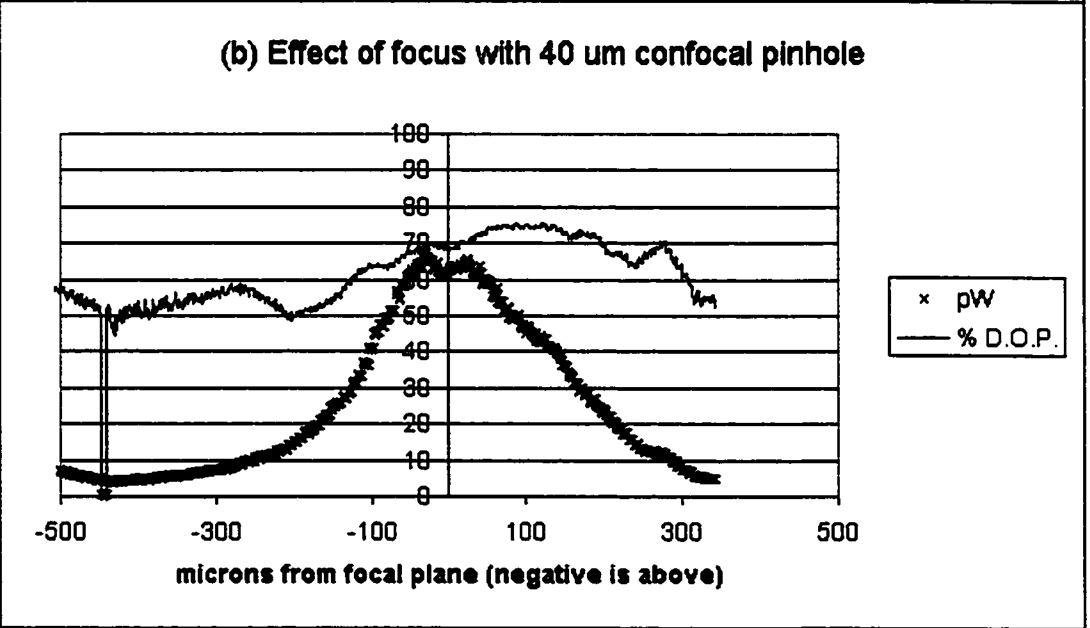

(b) Effect of focus with 40 um confocal pinhole

Figure 3.10. Effect of defocusing on collected light with 40-micron pinhole. In the absence of the confocal assembly (a), variability similar to that of Figure 3.9a is evident. With the assembly in place (b), the sensitivity of the polarization to misadjustment of focus is again reduced, and the FWHM of the total light intensity curve is reduced by 70% relative to the no-pinhole case. To achieve adequate signal level, however, a ~ 70-fold increase in incident laser power was required relative to that used with the larger pinhole.

successful use for similar SSFA application (Gough and Taylor, 1993). From the equations of Section 2.4, the sensitivity of the fluorescence anisotropy of a given fluorophore-macromolecule pair to a small change in viscosity can be determined to be

$$d\,r / d\,\eta = r_0\,\tau_f\,(\,\phi / \eta\,) / (\,\phi + \tau_f\,)^2.$$

where r is the SSFA, η is viscosity, r_0 is the anisotropy in the absence of rotational freedom, τ_f is the fluorescence lifetime of the fluorophore and ϕ is the rotational correlation time of the fluorophore.

The relation of ϕ to the hydrodynamic radius R_h of the macromolecule is such that d r / d η is maximized when

$$\delta\,(\,d\,r / d\,\eta\,) / \delta\,(R_h^3) = 0,$$

which occurs when

$$\tau_f = \phi.$$

Sensitivity is thus maximized when the rotational correlation time of the macromolecule matches the fluorescence lifetime of the fluorophore. Given that the fluorescence lifetime of fluorescein is ~ 4 ns, and assuming a specific volume of the hydrated macromolecule of ~ 0.75 cm^3 / gram, the use of a macromolecule of ~ 10 kDa is theoretically optimal.

A spherical 10 kDa dextran would be expected to have a rotational correlation time ϕ of ~ 4 ns (Luby-Phelps et al., 1986; Gough and Taylor, 1993). Dextrans of this size and smaller, however, tend to be ellipsoid rather than spherical (Granath, 1958;

Gekko, 1981). This results in an increase in ϕ relative to a spherical molecule of the same volume (van Holde, 1985).

The measured value for the SSFA of fluorescein attached to macromolecules, however, is typically lower than would be predicted for a given viscosity. One factor that may account for this apparent increase in rotational freedom is that the dextran may itself be internally flexible, allowing the measured ϕ to reflect only a local volume of the macromolecule (Lambooy et al., 1982; Steiner et al. 1983).

Another possible degree of freedom is that the FITC label may be free to rotate around its link to the dextran. The absorption and emission dipoles of fluorescein are essentially collinear with its three main aromatic rings, and therefore perpendicular to the single covalent bond of attachment to the dextran. If not otherwise sterically hindered, this rotation would serve to reduce the measured ϕ towards that of the label itself, particularly among the sub-population of macromolecules oriented with the bond in question parallel to the direction of incidence of the excitation light.

To investigate the contribution of this latter possibility, a fluorophore with an absorption dipole coaxial with its bond of conjugation was sought, which ideally would have similar spectral characteristics to fluorescein so as to minimize the necessity of additional filter sets. Just such a fluorophore was found in Molecular Probes' ATTO-TAG CBQCA. This reagent forms a cyanisoindole derivative with amine groups, with a dipole in line with its bond. This fluorophore is contrasted with fluorescein isothiocyanate in **Figure 3.11.**

The cyanoisoindole CBQCA derivative of a 10 kDa aminodextran was prepared by incubation of the dextran for 1 hour at room temperature with a two-fold molar excess of each of ATTO-TAG CBQCA derivatization reagent (Molecular Probes, Eugene, OR) and potassium cyanide. The SSFA of a sample of the derivative was measured

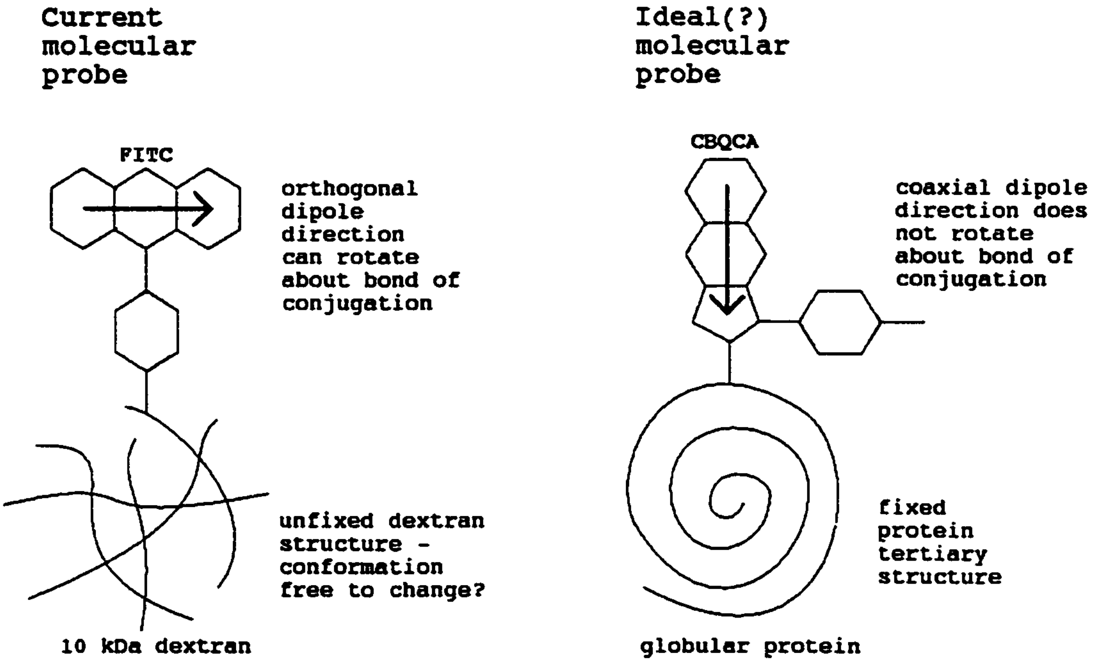

Figure 3.11. Comparison of molecular probe designs. In the current molecular probe, rotational freedom of the transition dipole of the fluorophore about its bond of conjugation to its associated dextran, coupled with the intramolecular flexibility of the dextran itself increase the apparent rotational freedom of the pair, decreasing the sensitivity of SSFA measurements. By using a fluorophore with a dipole coaxial with its bond of conjugation, coupled with a macromolecule with a more rigidly defined internal structure, fluorophore motion is made to vary in closer relation to the rotational diffusion of the entire molecular construct, resulting in more ideal sensitivity.

with the FANSOM system and independently by a commercial service using time-resolved fluorimetry (PTI, Inc., London, Ontario, Canada). The excitation and emission maxima were 468 and 560 nm, respectively, and the average fluorescence lifetime (determined by normalized integration of the exponential series fit; James and Ware, 1986) was found to be ~ 12.6 ns.

A ϕ of ~ 1.5 ns was found by the commercial service (see **Table 3.1**). This value is ~ 3-fold less than is expected of an inflexible macromolecule. The corresponding FANSOM SSFA measurement was higher; the source(s) of this discrepancy have since been identified will be discussed in detail in Section 4.2; for now only relative values are considered.

For comparison, the SSFA of a sample of a fluorescein-10 kDa dextran was measured with the FANSOM system and, again, independently by a commercial service (PTI, Inc., London, Ontario, Canada). As shown in **Table 3.1**, the SSFA of a FITC-labeled 10 kDa dextran was found by the commercial service to be ~ 0.045, corresponding to a rotational correlation time of ~ 0.5 ns. This suggests yet more rotational freedom of the fluorophore than would be expected (~ 7-fold). A quantitatively similar discrepancy was reported by Gough and Taylor (1993), suggesting that a protein (in their case, calmodulin) might not offer increased internal rigidity relative to the dextrans used here.

The increased apparent rotational freedom of the fluorescein-10 kDa dextran relative to the CBQCA-dextran suggests that the rotation of FITC about its bond of attachment is indeed a significant source of fluorophore mobility. That the CBQCA-dextran was still several fold more rotationally free than expected further suggests that the internal flexibility of dextrans is a significant source of fluorophore mobility, further compromising the sensitivity of the measured anisotropy of such a labeled macromolecule probe to changes in viscosity.

Table 3.1. Comparison of independently determined SSFA values. The SSFAs of a commercially available fluorescein-labeled 10 kDa dextran (FD10S, Sigma Chemical Co., St. Louis, MO) and of a custom-labeled 10 kDa dextran probe (ATTO-TAG) were measured by FANSOM and by a commercial fluorimetry service (PTI, London, Ontario). An SSFA value from the literature for fluorescein-labeled calmodulin (Fluo-CaM; Gough and Taylor, 1993) was also found. While FANSOM values at the time were found to be high (as discussed in Section 4.2), the relative values show the ATTO-TAG probe to be several-fold closer to theoretical ideality than the fluorescein-based probes (see "Ratio" column, indicating ratio of the measured to calculated phi), whose values were consistently some 7-fold lower than theoretically calculated values, both for FD10S and the published calmodulin analog data.

ATTO-TAG CBQCA-labeled 10 kDa aminodextran vs. FITC-10 kDa dextran

Method	**species**	**r0**	**r**	**tau f**	**phi calc.**	**phi**	**Ratio**
FANSOM	FD10S	0.396	0.109	4	4	1.52	0.38
PTI	FD10S	0.4	0.045	4	4	0.51	0.13
FANSOM	ATTO-TAG	0.377	0.12	12.6	4	5.88	1.47
PTI	ATTO-TAG	0.4	0.039	12.6	4	1.36	0.34
FAIM	Fluo-CaM	0.4	0.09	4	8.5	1.16	0.14

FITC-labeled dextrans of differing sizes were used for all following experiments reported herein due to their ready availability, stability, ease of use, and for reasons of experimental consistency during development (the chronology of the development of the CBQCA probe largely overlaps the other studies). It is clear, however, that a CBQCA-dextran will be the probe of choice for future experiments. The fluorescence lifetime of CBQCA suggests an optimal match with an internally fixed macromolecule of ~ 30 kDa; it is anticipated that conjugation to a larger dextran than has been used will result in yet further improvement over the FITC-10 kDa dextran.

4. FANSOM system characterization

4.1 Scans of gratings

To verify that the system was operating in a genuinely near-field mode, that the probes being used were of adequate quality, and that the positioning systems were accurate, NSOM images of diffraction gratings were obtained. Sample shear force and transmitted light line scans are shown in **Figures 4.1** and **4.2**, respectively. Muramatsu et al. (1999) considered the resolution of such profiles to be given by the lateral displacement necessary to produce a 20% to 80% rise in signal. By this criterion, the resolutions shown in these figures are 200 and 250 nm, respectively.

4.2 Preliminary SSFA trials

To determine whether the system could distinguish between samples of differing viscosities, solutions of 1 mM sodium fluorescein were prepared containing varying amounts of glycerol. Also, as a long rotational correlation time can derive from either high viscosity or a large macromolecule, the dual of the above experiment was later performed, i.e., measuring the SSFA of fluorescently labeled dextrans of varying molecular weight. These preliminary data are compiled in **Table 4.1**.

The agreement of experiment and theory is good for the highest viscosity, while the viscosity is overestimated for low viscosity samples. Both of the above trials were

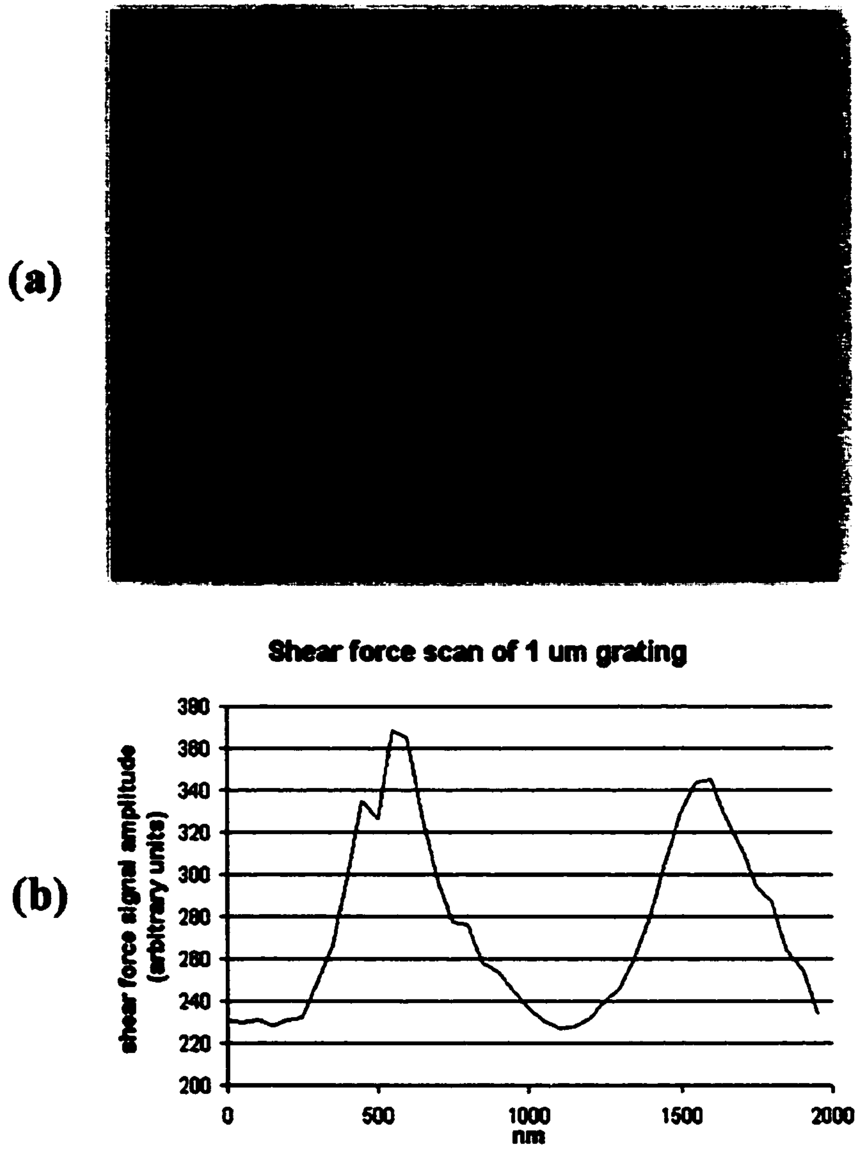

Figure 4.1. Shear-force scan of a 1-micron grating. As a test of the lateral resolution of the shear force system as implemented, a 1-micron gold-on-glass grating was scanned, and the horizontal distance over which a signal change from 20% to 80% of maximum occurred was determined (cf. Muramatsu et al., 1999). A scanning electron micrograph of the grating is shown in (a), from which it can be discerned that the regions of bare glass between stripes of gold are ~ 100 nm wide. A shear-force line scan perpendicular to the direction of the stripes (b) shows narrow peaks with a 1-micron spacing, corresponding to an increase in the freedom of the NSOM probe tip to vibrate over these regions relative to its surface-damped vibration over the gold stripes. Resolution is ~ 200 nm.

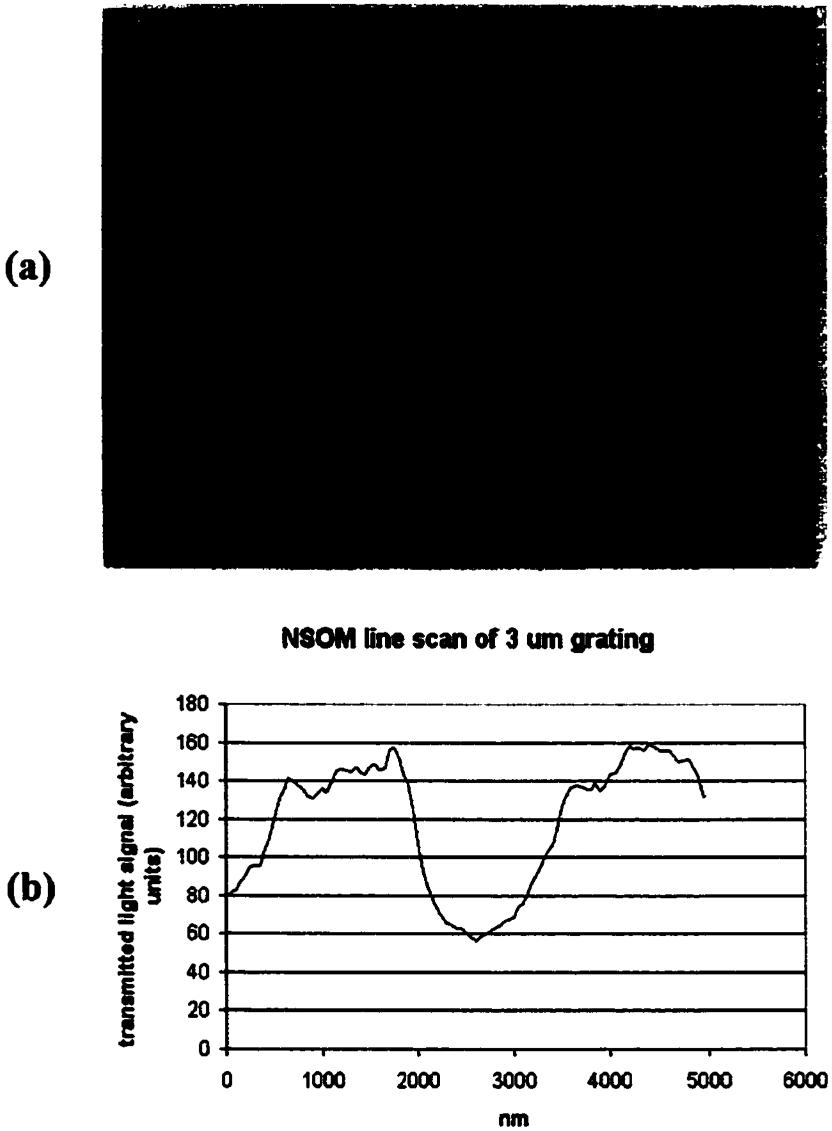

Figure 4.2. NSOM scan of a 3-micron grating. As a test of the lateral resolution of the NSOM system as implemented, a 3-micron holographic grating was scanned, and the horizontal distance over which a signal change from 20% to 80% of maximum occurred was determined (cf. Muramatsu et al., 1999). A scanning electron micrograph of the grating is shown in (a), from which it can be discerned that the periodicity of the grating has a duty cycle of ~ 50%. An NSOM line scan perpendicular to the direction of the grating stripes (b) shows peaks with a 3-micron spacing and ~ 50% duty cycle, with a resolution of ~ 250 nm.

Table 4.1: SSFA calibrations. SSFA measurements were taken in solutions of known viscosity and with the use of molecular probes of varying size. Values taken at high viscosity agree well with theory, while lower viscosity values are overestimated, as discussed in Section 4.2. Dextran-based molecular probes used show a much lower apparent molecular weight as determined by SSFA than expected, reflecting intramolecular flexibility as discussed in Section 3.8. The upper five rows of the table specify the conditions and raw data used to generate the lower five rows. The lower five rows compare apparent values for hydrodynamic radius, molecular weight, and viscosity with expected values.

Compilation of glycerol and dextran calibrations

estimated Rh of fluorescein (nm): 0.300
kDa/Rh(nm)^3 (from Luby-Phelps et al., 1986): 0.396
retrofit G: 0.842

% glycerol	dextran size	src. pol. (%)	r0	r	*r calc.*	*r corr.*	phi (ns)	Drot (ns^-1)
0	-	96.1	0.377	0.192	*0.003*	*0.000*	4.15	0.040
68	-	96.1	0.377	0.251	*0.042*	*0.069*	7.95	0.021
100	-	96.1	0.377	0.422	*0.343*	*0.345*	*-37.7*	0.004
0	70 kDa	97.7	0.386	0.088	*0.378*	*0.045*	1.18	0.141
0	2 MDa	97.7	0.386	0.095	*0.386*	*0.062*	1.30	0.128

% glycerol	dextran size	Rh app. (nm)	Rh calc. (nm)	MW app. (kDa)	MW calc. (kDa)	eta app. (cp)	eta calc. (cp)
0	-	-	0.300	-	-	152	1
68	-	-	0.300	-	-	291	18
100	-	-	0.300	-	-	1380	1487
0	70 kDa	1.05	5.61	0.46	70	-	1
0	2 MDa	1.09	17.1	0.51	2000	-	1

conducted before the implementation of the dichroic filter/beam dump excitation light exclusion scheme and before the significance of the spatial inhomogeneities of the PMTs used was fully appreciated; thus the corresponding channel offsets are likely to have been the source of the low viscosity overestimation. The effect of such offsets is shown in **Figure 4.3**.

The presence of a constant offset on one of the PMT channels becomes increasingly evident as fluorescence intensity becomes low relative to the offset. It is therefore especially important to correct for offsets when approaching a surface, as the decreasing pathlength of fluorophore will result in decreasing fluorescence, possibly producing an artifactual deviation in measured SSFA.

Another source of systematic error was the misestimation of the ratio G of the differing sensitivities of the PMT channels (cf. section 3.6). The effect of such misestimation is shown in **Figure 4.4**. The effect for SSFA values of 0.4 or less, to a close approximation, is simply to offset the measured SSFA from the actual SSFA by a constant value.

As shown in **Figure 4.5**, the above data sets are largely fit well by a model supposing excitation light leakage (of 5 $F\perp$ and 0.9 $F\perp$ for the glycerol and dextran data of **Table 4.1**, respectively) and with a recalculation of G (using the method of Dix and Verkman, 1990; G = 0.642). The apparent molecular weights of the dextrans, however, remain anomalously low. This phenomenon is likely due to intramolecular flexibility of the dextran, which can have branches of more than 50 glucose monomers in length (Granath, 1958). The rotational freedom of a fluorophore on such a branch might well reflect the size of the branch more than that of the entire macromolecule. The small overestimation of the viscosity of 68% glycerol may be due in part to the high sensitivity of viscosity to glycerol content at high percentages; back-calculating from the corrected anisotropy value suggests a 74% glycerol content.

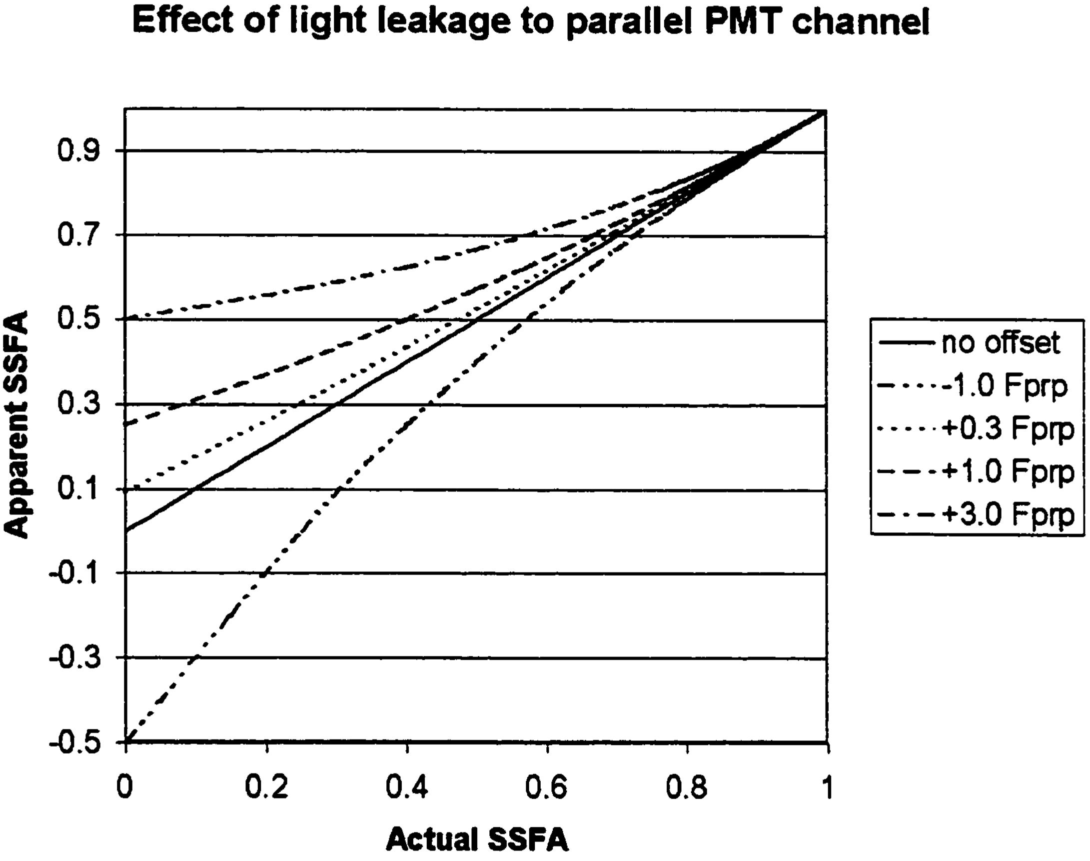

Figure 4.3. Effect of light leakage to parallel PMT channel. The calculated change in measured SSFA due to leakage of perpendicularly polarized fluorescence ("Fprp") into the channel intended for fluorescence of polarization parallel to the excitation polarization is shown. Excitation light leakage would appear as an apparent increase in parallel polarized fluorescence, resulting in deviations as shown. The primary effect of such perturbations is to offset low SSFA values away from zero.

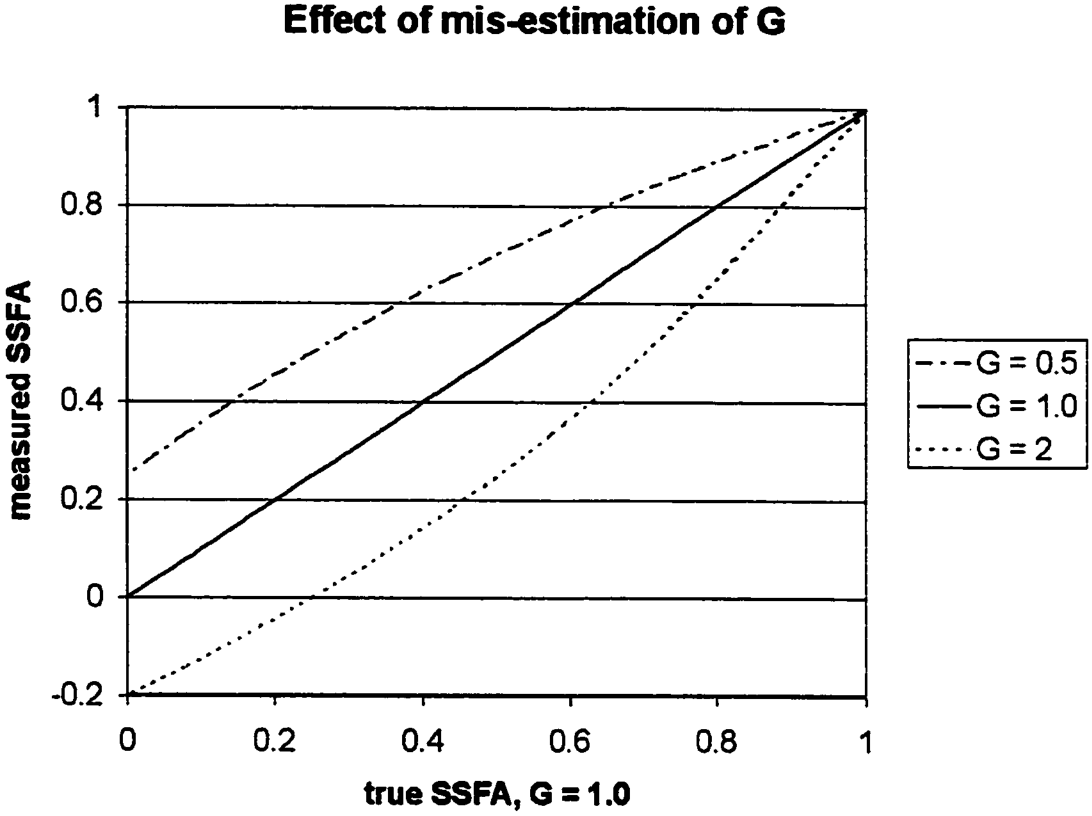

Figure 4.4. Effect of mis-estimation of G. The calculated effect of errors in the determination of the differential polarization channel sensitivity G is shown. For typical SSFA values (i.e., < 0.4), the primary effect of such error is to offset the measured SSFA by an approximately constant amount. Overestimation of G results in reduced apparent SSFA, while understimation has the opposite effect.

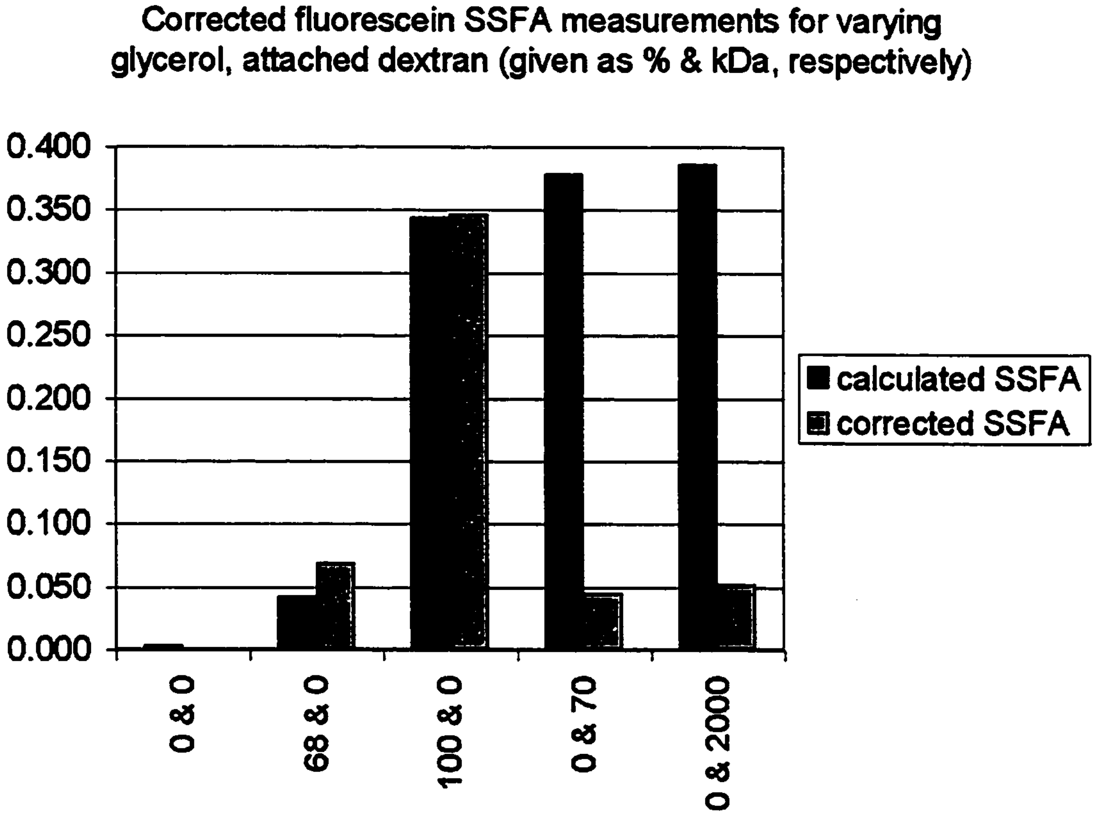

Figure 4.5. Corrected SSFA calibrations. SSFA measurements were taken in solutions of known viscosity and with the use of fluorescein-based molecular probes of varying size. After correction for excitation light leakage, SSFA values in glycerol solutions agreed well with theory, while measurements using larger molecular probes gave anomalously low values. These values were likely due to additional degrees of rotational freedom within the molecular probe as discussed in Section 3.8.

Since the system enhancements noted above, such corrections have been for the most part unnecessary.

4.3 Z-resolution

To determine the precision to which changes in microviscosity along a line paraxial with the probe can be determined, two vertical solution profiles approximating a step function were prepared and scanned.

The step profiles used were between solutions such that one solution contained fluorescein and the other did not, as described below. Using these preparations, the Z-axis profile of illumination intensity from the probe could be determined, from which the relative contributions of fluorophores at different distances from the probe tip could be calculated.

One step profile was an aqueous 1-mM sodium fluorescein solution ($\rho = 1$ g/ml) over a layer of immersion oil ($\rho \sim 1.3$ g/ml). For purposes of comparison and facilitation of experimental development, a scan-through of this sample was initially performed with a cleaved fiber as opposed to a tapered probe tip. The results are shown in **Figure 4.6a.**

The extinction coefficient of fluorescein at 488 nm is ~ 78,000 mol^{-1} cm^{-1}, which gives a calculated absorbance value of 78 cm^{-1} , or .0078 μm^{-1}, at a concentration of 1 mM. The fluorescence intensity would be expected to be proportional to the amount of excitation absorbed, and therefore the shape of the interface approach curve should be

(a) approaching immersion oil with cleaved fiber

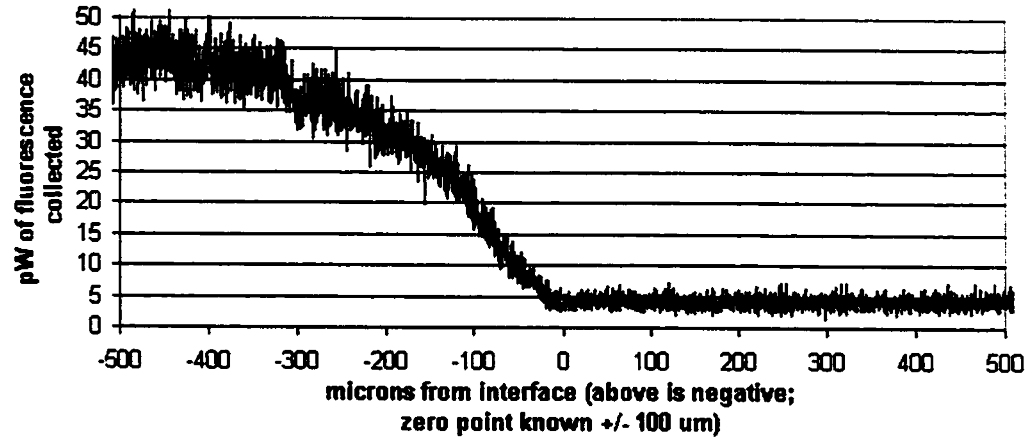

(b) approaching immersion oil with NSOM probe

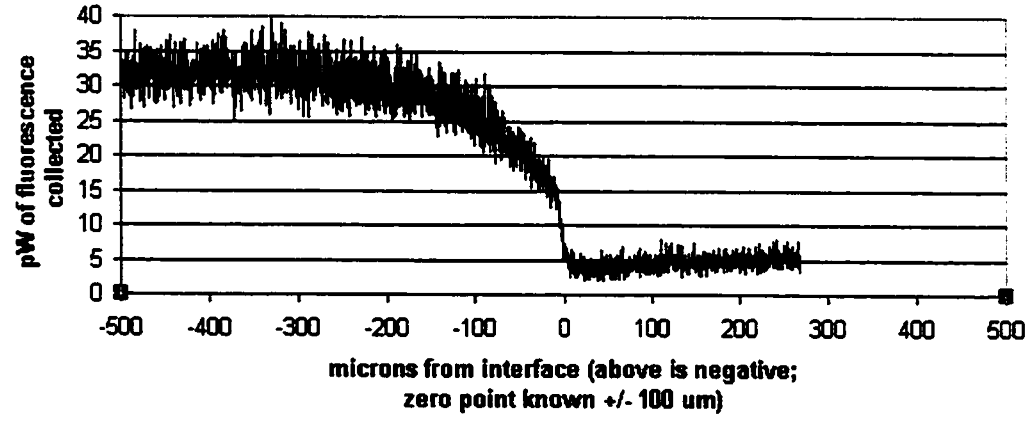

Figure 4.6: Immersion-oil approach with cleaved optical fiber vs. NSOM probe. (a) A cleaved optical fiber was advanced through an aqueous layer of 1-mM fluorescein towards a fluorescein-free layer of immersion oil. As the pathlength of absorbing fluorophore decreased, the fluorescence intensity dropped with a curve shape and rate essentially as expected. A non-zero baseline amount of fluorescence was noted, likely due to excitation light reflected from the cuvette bottom back into the fluorophore bath. (b) The experiment was repeated with an NSOM probe in lieu of the cleaved fiber. The fluorescence intensity dropped more abruptly than was observed with a cleaved-fiber ending, reflecting the contribution of the intense and localized near-field of the probe to the total signal. As in (a), a non-zero baseline amount of fluorescence was noted.

as predicted by this absorbance rate; it would be expected, over a distance of a few hundred microns, to curve from a baseline to an asymptote passing through zero. This is essentially what was found, though a basal level of background fluorescence is still seen after penetration of the immersion oil, probably arising from the reflectivity of the glass-air interface at the bottom of the cuvette used; the background was not seen upon repeating the experiment using pure water in lieu of fluorescein solution (data not shown).

The same experiment was conducted with an NSOM probe tip in place of the cleaved fiber end; the results are shown in **Figure 4.6b**.

The intensity of light in the near-field of an NSOM probe tip has been calculated to drop off with the 3.7th power of distance (Durig et al., 1986). The immersion oil interface approach curve would therefore be expected to drop off more sharply than that of the cleaved fiber, as the region immediately proximal to the probe should contribute a disproportionately large share of the total fluorescence collected. This drop is what was observed; the overall fluorescence drop-off occurred over approximately 1/5 the distance of the cleaved fiber case, including a large, abrupt drop to background levels in the last few points before penetration of the immersion oil.

The inverse experiment was also conducted, in which a glycerol solution ($\rho = 1.26$ g/ml) of 1 mM sodium fluorescein was approached through an organic overlayer (isooctane; $\rho = 0.691$ g/ml) devoid of fluorophore. The results for a cleaved fiber and an NSOM probe are shown in **Figure 4.7**.

The index of refraction of isooctane is 1.391, while that of glycerol is 1.4735. As the percent intensity reflectivity for normal incidence upon an interface between dissimilar materials is given by

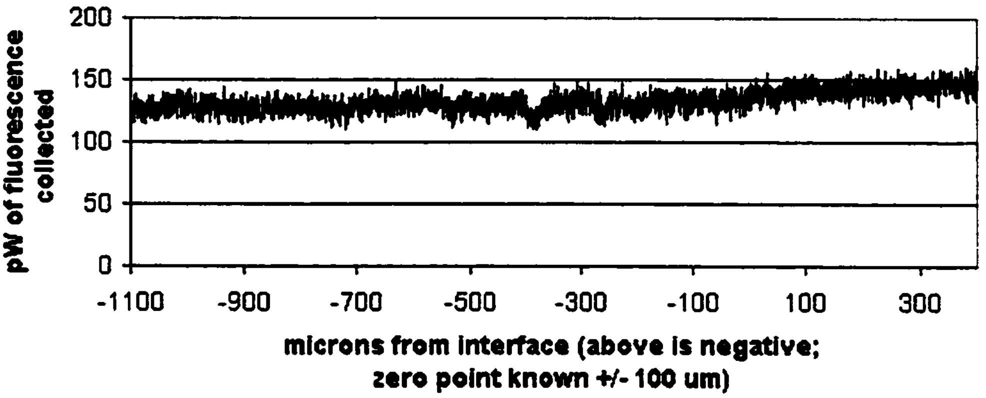
(a) Approaching aqueous fluorescein through isooctane with cleaved fiber

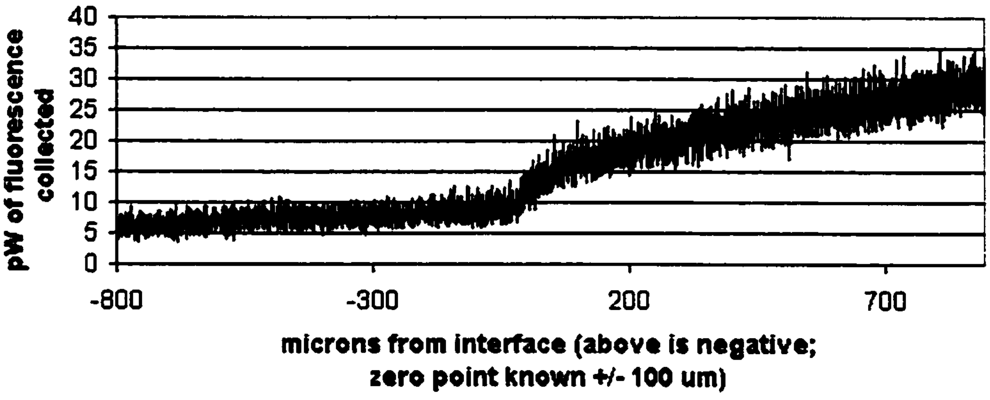
(b) Approaching aqueous fluorescein through isooctane with NSOM probe

Figure 4.7: Isooctane approach with cleaved optical fiber vs. NSOM probe. (a) The dual experiment to that of Figure 4.6a was performed, approaching a solution of 1 mM fluorescein in glycerol through an overlayer of fluorophore-free isooctane. A minor increase in fluorescence intensity was seen upon entry into the fluorophore, likely reflecting the tendency of the isooctane-glycerol meniscus to lens excitation light away from the objective lens. (b) The experiment was repeated with an NSOM probe in lieu of a cleaved fiber. A jump in fluorescence intensity was seen upon entry into the fluorophore, reflecting the contribution of the intense and localized near-field of the probe to the total signal.

$$\% \text{ reflectivity} = 100 \times (n_1 - n_2 / (n_1 + n_2))^2,$$

the isooctane - glycerol interface is anticipated to be ~ 0.08% reflective. A slight increase in collected light would thus be expected upon penetration of this interface. Also, the difference between the fiber core - isooctane interface reflectivity (~ 0.14%) and that of the fiber core - glycerol interface (~ 0.008%) suggests a further increase in collected light. Perhaps most significant, however, is that the interface was not flat, resulting in the lensing of light away from axial until the interface was penetrated.

An increase of ~ 8% was observed upon interface penetration in the case of the cleaved fiber, consistent with the latter phenomenon. This jump was followed by a gradual increase, as an increasing amount of the omnidirectional fluorescence fell within the NA of the objective.

In the case of the NSOM probe tip, an abrupt increase would be expected as the intense evanescent region of the near-field enters the fluorophore, and this is what was observed, along with a somewhat more rapid increase in collected light with further approach, likely due to the increased angle of light dispersal at the tip relative to that of the cleave.

The experimental parameters generating **Figure 4.6b** most closely resemble those anticipated for a typical application of the FANSOM system and can be used to estimate what the system's response to a step change in SSFA would be; in essence, this response defines the vertical axis point spread function of the system. In **Figure 4.8**, the data of **Figure 4.6b** have been rolling averaged (over 15 μm of pts) and converted into expected SSFA values for a free fluorescein to completely fixed fluorescein step. The SSFA was determined by estimating the baseline fluorescence levels long before and just after interface penetration and mapping the signal level at each point within this range to the corresponding percentage of maximum

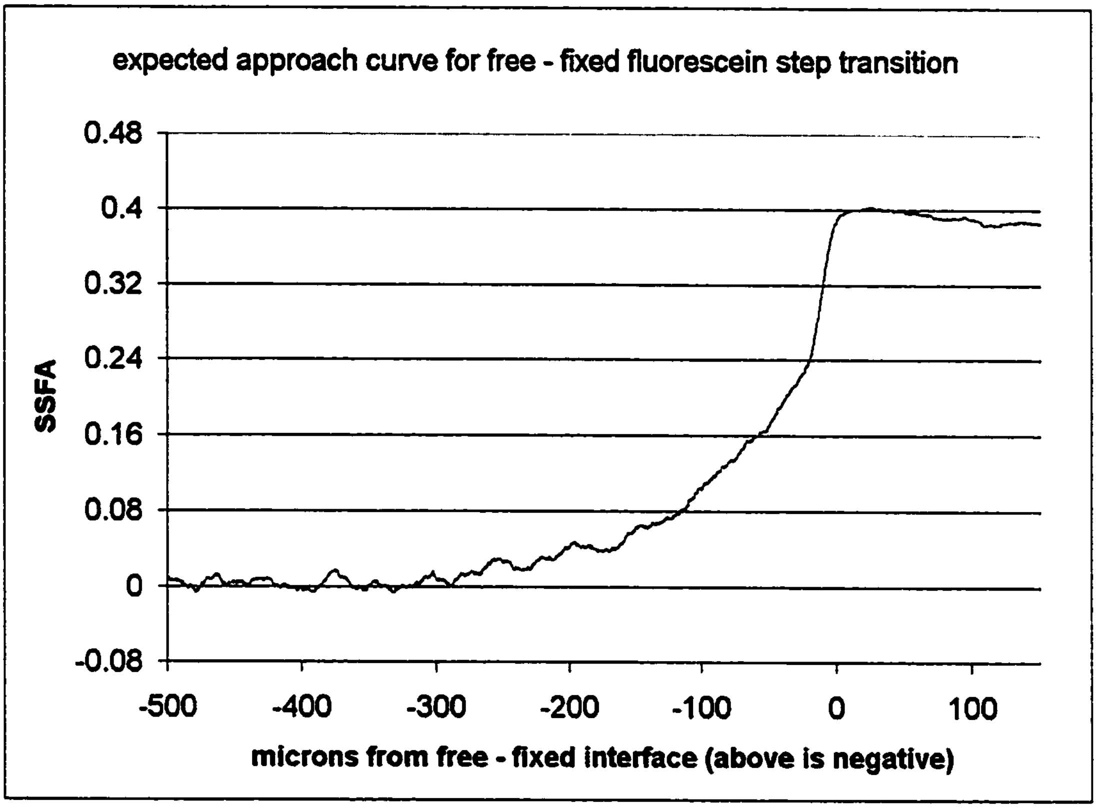

Figure 4.8. Vertical FANSOM system response. The data of Figure 4.6b have here been used to anticipate the shape that a FANSOM approach curve would take if the probe were advanced through a step change in SSFA from completely free to completely fixed fluorophore. This curve approximately defines the vertical axis point spread function of the system (obtained via deconvolution of this curve from the step function).

fluorescence signal contributed by the pre-step free fluorescein. The remainder of the illumination was modeled to be absorbed and re-emitted by completely fixed fluorescein. The resulting curve approximately indicates the step response of the system, from which the system transfer function may be obtained. This transfer function may then be deconvolved from long vertical scans to obtain the corresponding actual SSFA profiles.

5. SSFA in gels

5.1 SSFA in dense polyacrylamide

To discern initially whether the proximity of surfaces and/or immobilized water might indeed measurably retard the rotation of labeled macromolecules, an extreme case was used. Retarded diffusion and/or restriction of water rotational freedom has been found in polyacrylamide gels (Pavesi and Balzarini, 1996; Murase and Watanabe, 1989). A cleaved fiber end was used in lieu of a probe tip to measure the bulk SSFA of polyacrylamide throughout gelation. The data obtained are summarized in **Figure 5.1.**

An increase in apparent microviscosity was noted for both gel compositions, being larger in the more highly crosslinked gel (30% acrylamide / 2.7% bisacrylamide). If the SSFA increase were due to binding of the fluorescein to the gel structure, this fraction would be expected to photobleach quickly under the intense illumination of the probe tip, resulting in a SSFA drop to a basal level reflecting free fluorescein. No such drop was observed (signal change < 1% over several minutes; data not shown). It is therefore likely that some aspect of the gels reduced the rotational freedom of the fluorophores via a ranged effect as opposed to direct binding.

One possible explanation of the increased apparent microviscosity is predicted from classical hydrodynamics. Water sheared between a rotating molecule and a static surface such as a strand of the gel in question would generate larger drag forces than water sheared only by the molecule rotating amidst bulk water (Howard, 1993). For this effect to result in the ten-fold difference in viscosity found, however, the fluorescein molecules would have to remain, on average, within a nonsensical 10 pm from a surface.

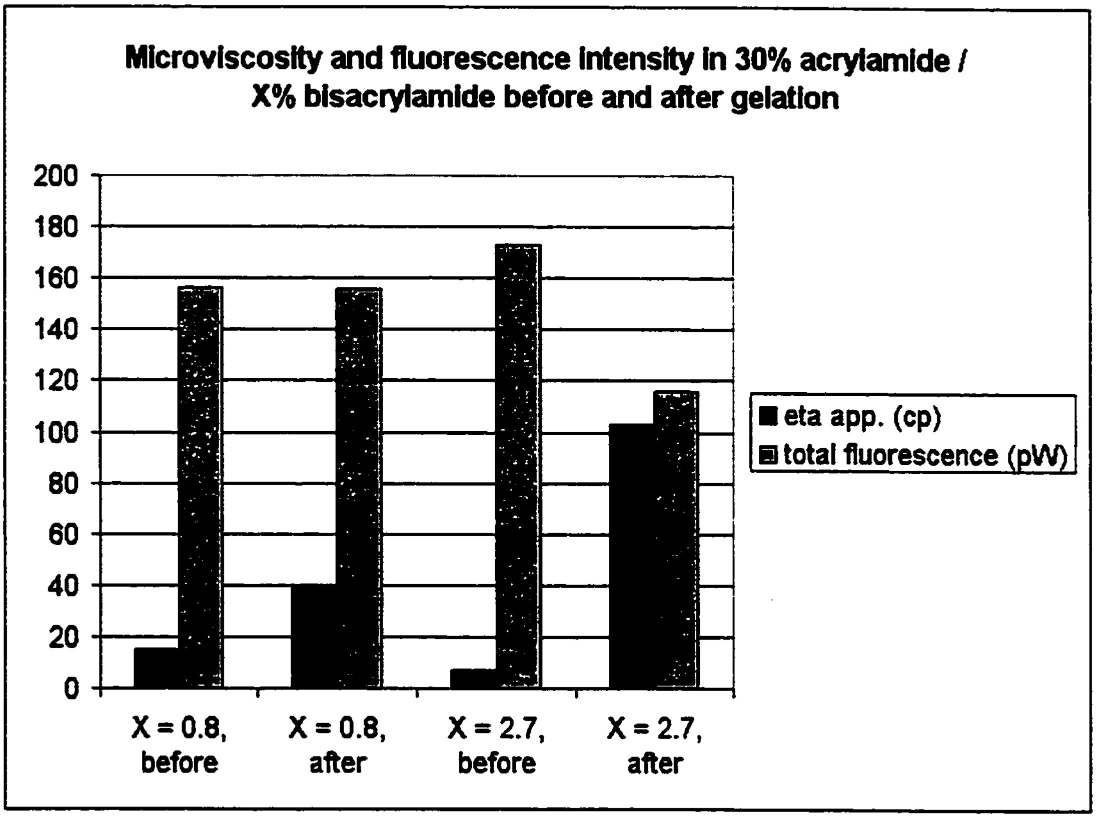

Figure 5.1. Microviscosity before and after polyacrylamide gelation. The apparent microviscosity as measured by SSFA of free fluorescein ("eta app.") in a 30% acrylamide preparations increased abruptly upon gelation, both in moderately and highly crosslinked gels (0.8% and 2.7% bisacrylamide content, respectively). The change was more pronounced in the more highly crosslinked gel. This phenomenon was not accompanied by photobleaching, suggesting a ranged interaction between the molecular probe used and the interstitial surfaces of the gel. Fluorescence intensity was also observed to drop in the case of the more highly crosslinked gel, although the cause of this phenomenon remains unclear.

These data are suggestive of a water-mediated inhibition of rotational freedom.

A drop in fluorescence intensity during gelation was also noted in the case of the 30%/2.7% gel. This drop was not observed in the case of the 30%/0.8% gel, suggesting that this result is dependent upon the degree of cross-linking rather than chemical involvement by the gel constituents (e.g. quenching, oxidative photobleaching, etc.).

5.2 SSFA in agarose gels

Derbyshire and Duff (1974) found using NMR that 0.59 g of water were in a "bound" state for every gram of agarose in gels from 0.9 to 18%. This systematic study provided a useful basis for comparison with viscometric results. To further determine if the SSFA signal was correlated with bound water, SSFA measurements were taken in a similar range of agarose gels. The resulting data are shown in **Figure 5.2**.

A rough proportionality was found in the relationship between % agarose and measured microviscosity ($R^2 = 0.7435$ for a zero-intercept, linear fit), with a slope of ~ 2 cp per % agarose. This slope corresponds to a ratio of 1 cp of microviscosity per 0.3% water bound. A causal relation between these parameters remains to be demonstrated.

How might bound water result in enhanced microviscosity?

Hjerten and Eriksson (1984) determined the effective pore size of agarose gels of varying concentration. Their data, in conjunction with simplifying assumptions about the small-scale geometry of agarose gels, may be used to construct a simple, quasi-

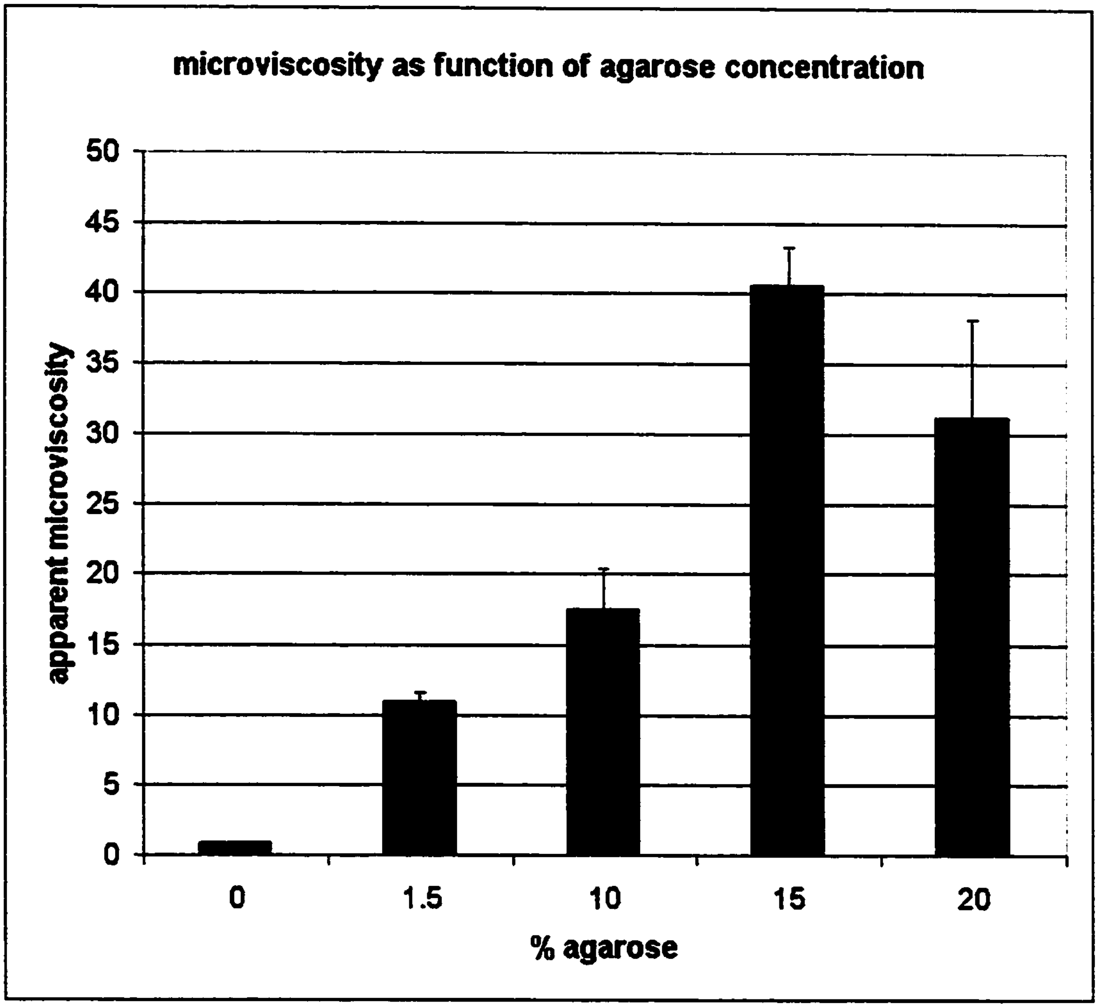

Figure 5.2. Microviscosity as function of agarose concentration. The apparent microviscosity as measured by the SSFA of free fluorescein ("eta app."; shown with 1 std. err.) was determined for agarose gels of varying concentration. An approximate ratio of 2 cp per % agarose was found. Combined with previous NMR measurements of bound water in similar gels (Derbyshire and Duff, 1974), this corresponds to ~ 1 cp per 0.3% water bound.

quantitative model of the interstices of agarose gels. From this model, an interstitial surface area may be estimated, which in turn facilitates estimation of the degree to which water may be bound. Such a model is shown in **Figure 5.3**. The model shown assumes a regular, repeating cubic structure of agarose with a specific volume equal to that of water.

One hypothesis is that the bound water previously measured is simply plated evenly upon the surfaces of the interstices of the agarose, and shears less readily than bulk water, producing increased microviscosity. The model suggests that the surface area of the agarose-water interface is somewhat insensitive to % agarose, changing only ~ 2-fold over a 4-fold variation in % agarose, arguing against this hypothesis. It is still possible, however, that the surface binding is cooperatively non-linear, such that the observed linear relation between % agarose and bound water is restored.

Another hypothesis is that the bound water exists within the agarose of the matrix itself as opposed to the interstices thereof. This placement would reproduce the observed linear relation between % agarose and bound water. In this case, measured microviscosity might reflect an average of two populations of fluorophore-macromolecule probes; one free in the bulk, and one partially soluble and immobilized within the agarose.

Finally, one other experiment was performed. To compare the differential solvation and/or efficiency of the fluorophore within and outside of the gel, the first 20% agarose preparation was refrigerated in the cuvette for 24 hours before measurement to allow the fluorescein within it to equilibrate with excess solution above it. After this time, the fluorescence intensity at more than 1 mm above the agarose was 162 pW, while that in the agarose was 191 pW. The sign of this fluorescence change was the opposite of that observed in polyacrylamide, and the opposite of that expected from simple volume exclusion by the agarose gel. It may be that both types of gel somehow

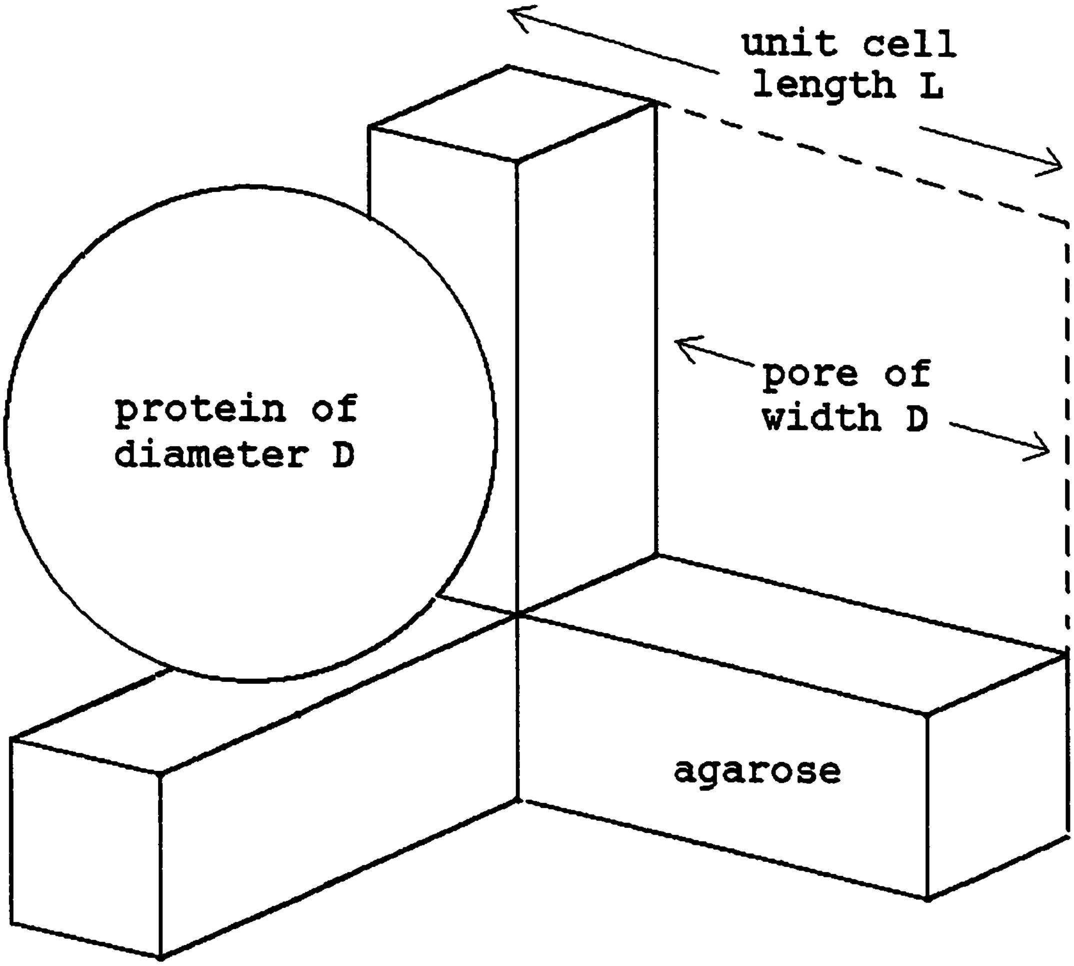

% agarose	excluded MW	protein D (nm)	unit cell L (nm)	area/unit cell (nm^2)
5	1000000	13.3	15.5	0.091
9	600000	11.3	13.8	0.131
12	450000	10.2	13.1	0.156
20	280000	8.73	12.3	0.200

calculations based upon pore size data of Hjerten & Eriksson (1984) Anal. Biochem. 137:313

Figure 5.3. A simplified model of agarose gel structure. Assuming a regular, cubic structure of the interstices of an agarose gel, data on agarose gel pore size (Hjerten and Eriksson, 1984) may be extended to the analysis of hypotheses concerning water binding to interstitial gel surfaces.

exhibit enhanced fluorophore solvation, but this effect was obscured by the short timescale and/or dynamic nature of the former experiments.

The differential PMT channel sensitivity G for these data was determined by the method of Dix and Verkman (1990).

In sum, these data suggest a correlation between bound, and thus vicinal, water and microviscosity.

6. FANSOM over putative structuring surfaces

To investigate the ability of surfaces of varying hydrophilicity to induce vicinal water with altered microviscosity, FANSOM measurements were taken over the surfaces described below.

6.1 Glass

Initially, a retraction from the bottom of a simple glass cuvette was performed while monitoring SSFA and collected fluorescence intensity. Shear force was used to determine the point of zero distance from the glass to within ~ 10 nm. The data are shown in **Figure 6.1.**

No change in SSFA was noted, while the amount of collected fluorescence dropped off as expected over the last few hundred microns, as was the case in the above immersion oil approaches.

The value of SSFA, or r, was ~ 0.03 +/- 0.03. From the equations of section 3.8, it can be found that for the case of free fluorescein in aqueous solution, $d\,r / d\,\eta \sim 0.003$ / cp, corresponding to an error margin of ~ 10 cp.

These data suggest that if ordinary glass influences the viscosity and/or fluorescein solubility in its immediate vicinity, it is to a smaller degree than ~ 10 cp of viscosity change over ~ μm distances.

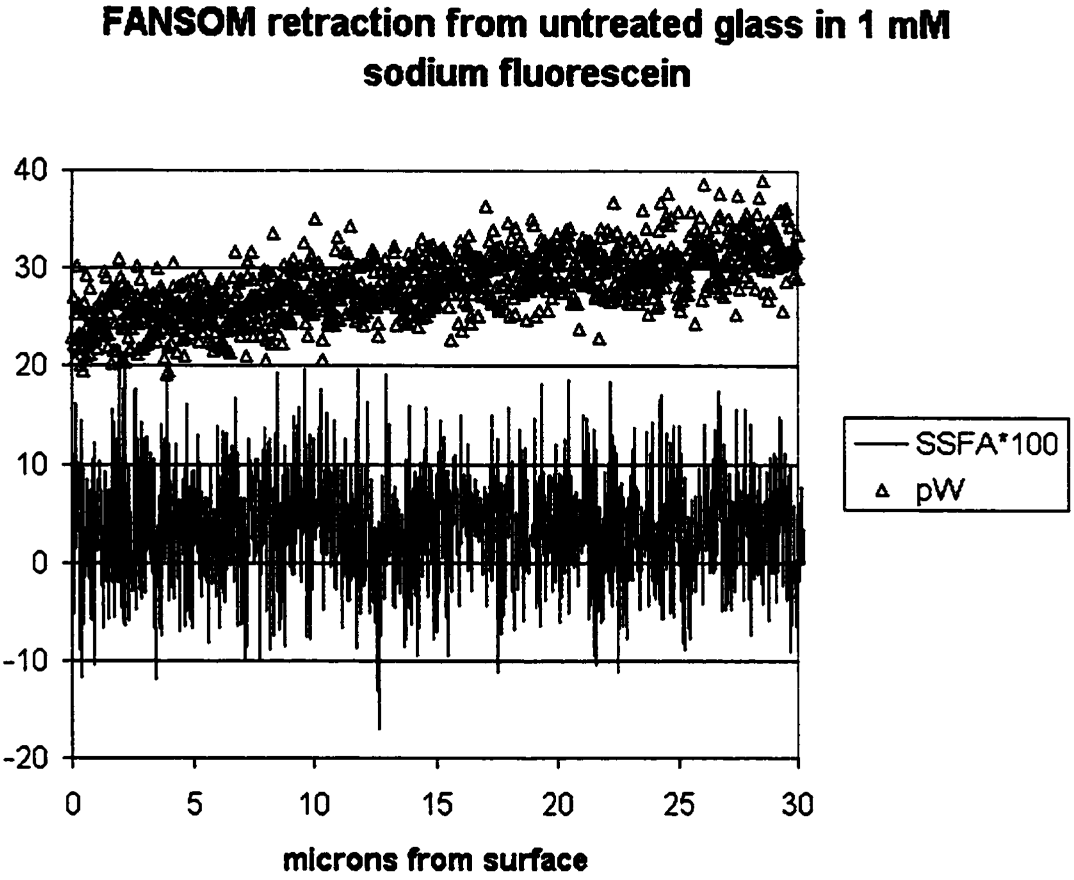

Figure 6.1. FANSOM over untreated glass. After bringing the NSOM probe into close proximity with the glass bottom of a cuvette using shear force as a guide, the probe was gradually retracted from the surface while concurrently monitoring SSFA and total fluorescence intensity. Free fluorescein was used as the molecular probe. No change in SSFA with distance was noted, with an error margin of ~ 10 cp. Total fluorescence intensity increased with the increasing pathlength of fluorophore essentially as expected, though displayed a significant non-zero apparent baseline amount, likely due to non-excitation light leakage.

6.2 Sigmacote®

The same experiment was later conducted after silanization of the glass cuvette interior with Sigmacote®. The results are shown in **Figure 6.2a**. **Figure 6.2b** shows a rescaled view of the last 10 nm of approach. Again, no change in SSFA was noted. The rate of retraction was increased at ~ 0.4 µm from the surface.

The light intensity decreased slightly faster in the last ~ 0.2 µm from the surface, roughly corresponding to the extent of the near-field. A drop-off is expected due to the higher intensity of light within the near-field (cf. **Figure 4.7**), though other factors may contribute. An intriguing possibility is the exclusion of fluorophore from the surface by ice-like water structure induced by the hydrophobic surface (cf. Vogler, 1998). From this experiment alone, however, it is not yet possible to distinguish this possibility from more mundane explanations, including occlusion by the probe tip of excitation light reflected from the water/cuvette interface back into the bulk.

An SSFA of ~ 0.06 +/- ~ 0.01 was observed. The sensitivity was enhanced relative to the case of free fluorescein by the substitution of FITC-10 kDa dextran. Using the value of ϕ for this species shown in Table 3.1 (PTI value), $d\,r / d\,\eta$ can be calculated to be ~ 0.08 / cp, corresponding to an error margin of ~ 0.1 cp.

These data suggest that if Sigmacote® influences the microviscosity in its immediate vicinity, it is to a smaller degree than ~ 0.1 cp over distances of ~ 10 nm.

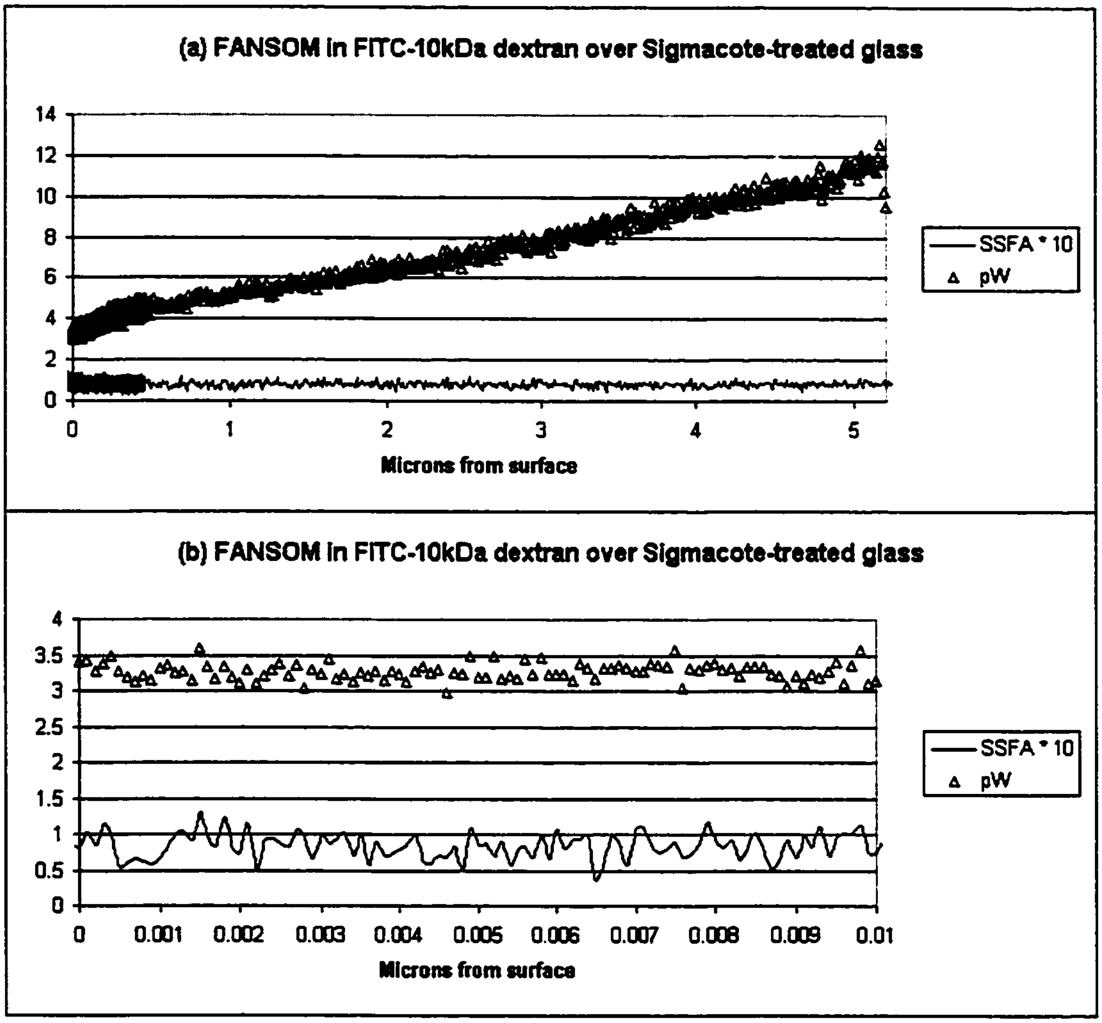

Figure 6.2. FANSOM over Sigmacote®-treated glass. After bringing the NSOM probe into close proximity with the glass bottom of a cuvette using shear force as a guide, the probe was gradually retracted from the surface while concurrently monitoring SSFA and total fluorescence intensity. A fluorescein-labeled 10-kDa dextran was used as the molecular probe. No change in SSFA with distance was noted, with an error margin of ~ 0.1 cp. Again, total fluorescence intensity increased essentially as expected with a short (~ 0.2-micron) region of more rapid change at the surface, roughly corresponding to the high-intensity near-field region of the probe's emission. (a) shows several microns of the retraction, while (b) shows the initial 10 nm in closer detail. The apparent discontinuity at ~ 0.4 microns corresponds to an increase in retraction rate.

6.3 Cleaved mica

The same experiment was then conducted after securing a small sheet of freshly cleaved mica of ~ 100-μm thickness to the inside of the bottom of the cuvette with a small drop of immersion oil.

Cleaved mica is uniformly hydrophilic, to the point of passing the "steam test" (cf. Pashley and Kitchener, 1979). Most materials held over boiling water will "fog up" as microbeads of water form, either nucleated by surface contaminants or due simply to hydrophobicity of the surface. In contrast, highly clean, hydrophilic surfaces such as cleaved mica and exhaustively polished and cleaned quartz form a continuous film of water, visible only via the subtractive coloration characteristic of thin films. Complete coverage of mica by water occurs spontaneously in humidity as low as 37%, with the thickness of the water layer increasing with increased humidity (6 nm at 37%, 13 nm at 52%; Okajima and Hirotsu, 1997; Davy et al., 1998) .

Mica is, however, a birefringent material. What effect is this expected to have upon a FANSOM measurement?

In a birefringent material, the retardation of extraordinary-axis aligned polarized light relative to ordinary-axis aligned light is given by

$$N = b\,x / \lambda,$$

where N is the number of wavelengths of retardation, b is the birefringence of the material, x is the thickness of the material traversed, and λ is the wavelength of light used. The birefringence of the type of mica used (Muscovite) is ~ 0.04; therefore N in the case of this experiment is ~ 8. Given only one significant figure of known precision, it is possible that the mica could have a tendency as great as a quarter-wave plate to circularize incident polarization, making the fluorescence from even a completely fixed molecular probe appear freely mobile.

Full circularization, however, is only achieved when fully half of the incident light is retarded by one-quarter wave; this condition can readily be avoided by the alignment of either optical axis with the incident polarization. A suitable orientation of the mica sheet was determined by rotation of the mica sheet between crossed polarizers illuminated by HeNe laser light. Extinction indicated an orientation of non-circularization.

Despite this precaution, it is likely that some depolarization due to the birefringence of the mica occured, and that FANSOM measurements made above the mica show an artificially lowered degree of anisotropy. Nonetheless, a semi-quantitative investigation of changes in FANSOM signal in the vicinity of this highly hydrophilic surface remained possible.

A representative set of obtained data is shown in **Figure 6.3**. As in **Figure 6.2a** of the previous section, a drop off in total fluorescence intensity is noted over a similar vertical range (~ 150 nm), with the same probable cause.

Perhaps most interestingly, a drop was also noted in the SSFA, curving down from an asymptotal maximum of ~ 0.06 over a range of several microns (shown magnified in the figure as "SSFA*300", ~ 18). This apparent increase in viscosity is consistent with an increased density of water molecules at the hydrophilic surface, as described by Vogler (1998). In this model, water-surface interactions dominate over water-water interactions, resulting in an increased density of water relative to a more ordered, ice-like structure. The ~ micron range observed herein, however, is very much greater than would be expected from the model described by Vogler; why structural disorder should propagate beyond a few water layers, much less beyond the

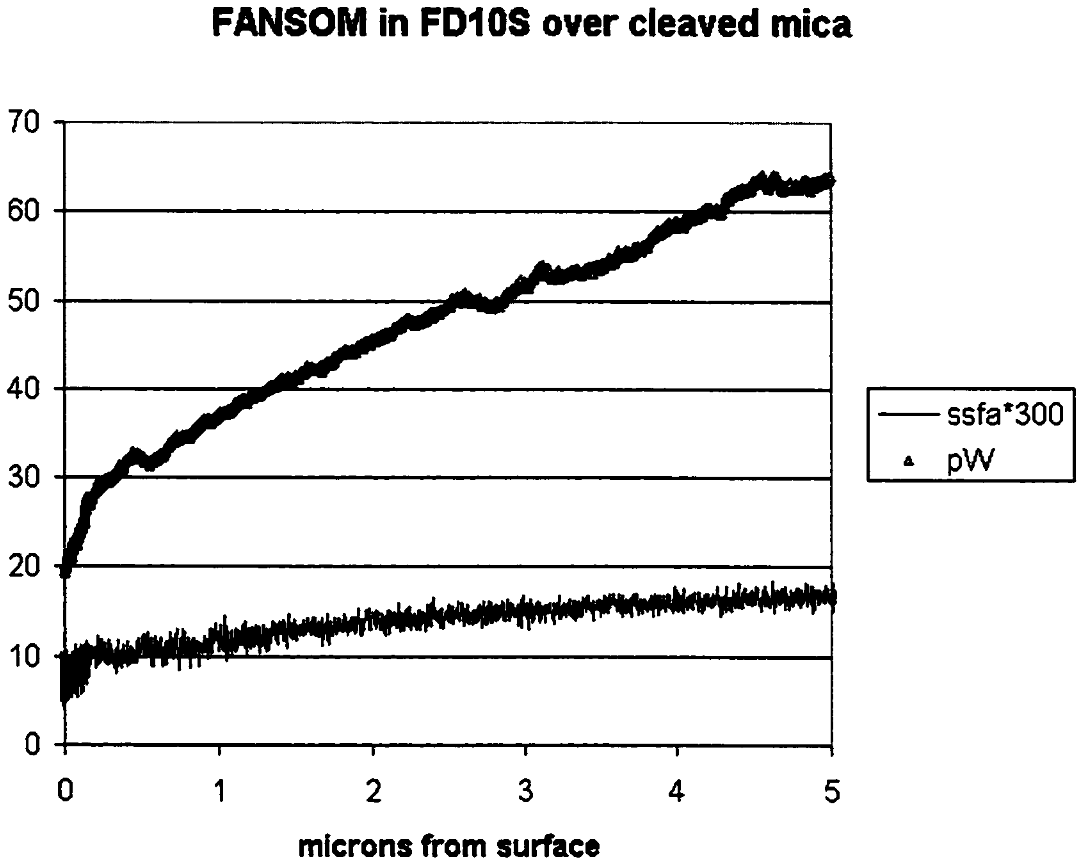

Figure 6.3. FANSOM over cleaved mica. An increase in SSFA with distance was noted qualitatively, possibly indicating increased water density at the mica surface. After bringing the NSOM probe into close proximity with a sheet of cleaved mica using shear force as a guide, the probe was gradually retracted from the surface while concurrently monitoring SSFA and total fluorescence intensity. A fluorescein-labeled 10-kDa dextran was used as the molecular probe. Total fluorescence intensity increased essentially as seen in Figure 6.2. The apparent discontinuity in the SSFA signal at ~ 0.1 microns corresponds to an increase in retraction rate.

~ 100 nm range of putatitive ordering (hydrophobic forces; Israelachvili and Adams, 1976; Israelachvili and Adams, 1978) is difficult to imagine.

One possibility is that the crystal spacing of the mica coincides with that of optimal water structure, serving to order rather than disorder the adjacent water. The apparent increase in viscosity could then correspond to decreased mobility of the water rather than an increase in density, while the increased range relative to previous studies could be attributed to a cooperativity inherent in the regularity of the mica sheet; previous comparable studies finding shorter-range structure used a much smaller area of mica (Israelachvilli and McGuiggan, 1998).

7. Biological applications of FANSOM

7.1 Scans of myofibril bundles

The myofibril was chosen as an initial biological specimen for FANSOM application due to its highly regular structure and our collective experience, as a laboratory, with this preparation.

Five years ago in this laboratory, it was found that shear force images of myofibrils and myofibril bundles showed three mysterious bands per sarcomere, as shown in **Figure 7.1** (Seibel, 1996; Seibel and Pollack, 1997). It was not clear at the time if the bands were due to stiffness changes, an optical artifact of the trans-sample shear force scheme used at the time, or local viscosity variations.

The variations were noted to be detectable some 500 nm from the sample. It is unlikely that these variations were due to stiffness changes, as this range is approximately an order of magnitude greater than the longest shear-force interaction distances reported in the literature.

Viscosity variations are also an improbable causative agent. The symmetry of the myofibril would be expected to produce a radially symmetric variation were such a variation to exist, and the pattern was observed only above the myofibril, and not beyond its lateral boundaries. An asymmetry is introduced by the glass substrate beneath the myofibril, though as noted in the featureless ordinary-glass viscosity profile of **Figure 6.1**, this coincidence is likely insufficient to account for the observed result.

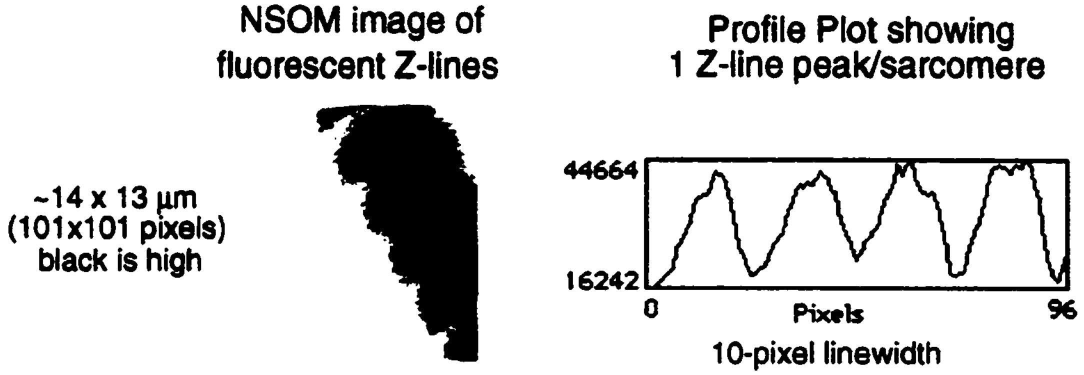

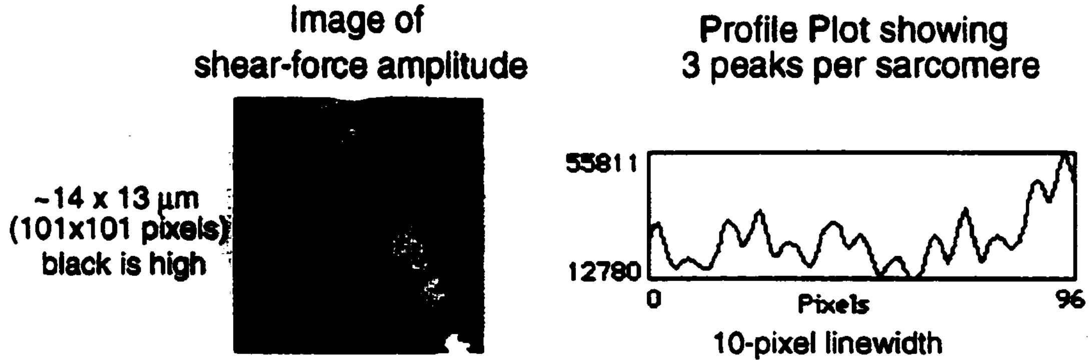

Figure 7.1. Thick myofibril bundle scan of Seibel (1996). A myofibril bundle is shown with immunofluorescently labeled Z-lines (above) and as imaged by shear-force. Three peaks per sarcomere are noted in the shear-force image. The shear force system used was trans-sample; an image of the probe tip above the sample was formed by the light collection objective below the sample. This image of the tip was projected upon a pinhole, and as the probe vibrated, the amount of light traversing the pinhole to be detected by a PMT varied, providing a measure of tip vibration.

Still, Cleveland et al. (1976) found it necessary in their NMR studies to postulate that 37% of water in muscle exists in a bound state to account for their data. While likely not of 500 nm extent, could it be that water binding does extend beyond the boundaries of individual myofibrils?

The myofibril bundle experiment of Seibel (1996) was reproduced, with two differences: (1) the optical path of the new shear force system was implemented above the sample and perpendicular to the optical path of the microscope, and (2), FANSOM measurements were taken in lieu of simple fluorescence intensity data points. If the bands persisted under the new shear force system, the trans-sample artifact would be excluded, while the FANSOM results could give information about viscosity variations independently of myofibril stiffness.

In the experiments described below, the NSOM probe was extended to the cuvette bottom and retracted to 1-10 μm from the surface before repeated translation of the sample under the tip. Though the rigid cuvette bottom could be located with certainty even under solution using shear force, the point of contact with the relatively compliant myofibrils had to be inferred less directly. The height of retraction was chosen to coincide with the apparent size of the myofibril or bundle thereof as viewed in brightfield. If translation of the myofibril under the probe tip via manual coarse adjustment of the stage position produced no visible perturbation of the myofibril(s), it was assumed that the height was sufficient to clear them. The bundle was then repeatedly scanned, and the plane of the scan was advanced toward the myofibril(s) by ~ 10-100 nm between each scan. Contact was then judged to correspond to the first scan showing distortions characteristic of the snaking raster pattern used for the scans (cf. Seibel, 1996). Myofibrils were prepared by the method of Bartoo et al. (1993).

Figure 7.2 shows a cartoon representation of an NSOM tip scanning at a constant height just over a myofibril. When the probe is further away laterally than ~ 1 μm

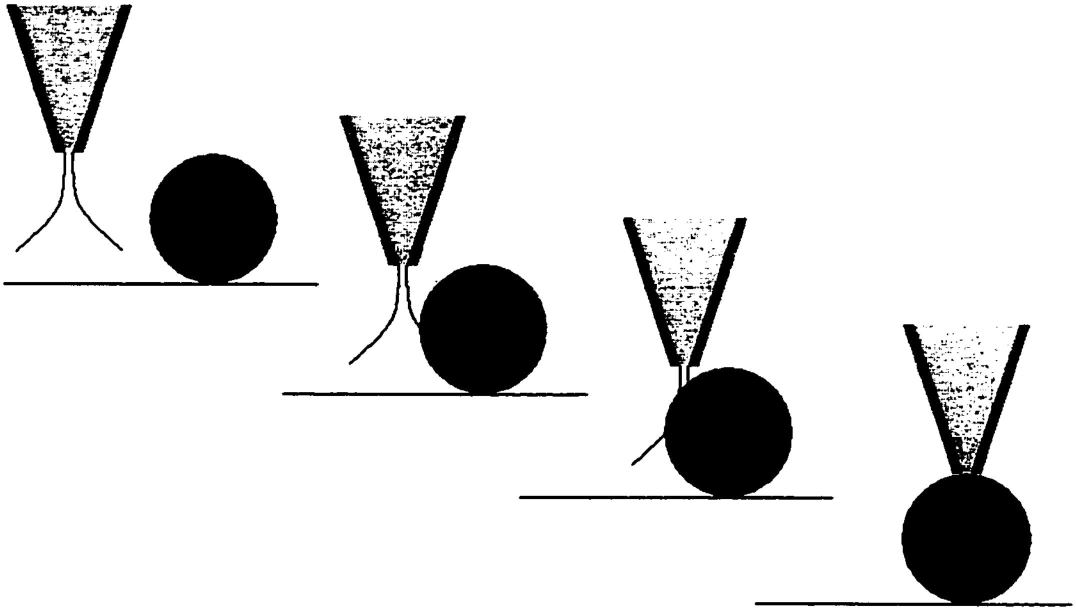

Figure 7.2. Constant height scanning. As an NSOM probe scans closely across a myofibril, the degree of interaction of the probe's near- and far-fields with the myofibril varies. Within ~ 1 diameter of the myofibril, diffuse far field light begins to interact with the myofibril. Resolution increases as the probe-myofibril distance decreases, gradually achieving near-field resolution. This radial variation in the resolution of constant-height scanned myofibrils gives their bands a rounded appearance in resulting images.

from the myofibril, little change to the FANSOM signal is expected, with the exception of a small amount of specular reflection from the underlying substrate that may reach the myofibril. As the probe continues to draw near, a portion of the probe's far-field overlaps the myofibril, and the signal begins increasingly to reflect that of the myofibril. As the probe becomes completely occluded, essentially the entirety of the light is influenced by the myofibril, while the near-field of the probe only gradually overlaps. Finally, with the probe directly over the midpoint of the myofibril, the majority of light collected has passed through the portion of the myofibril within the near-field, resulting in a maximum of signal-to-noise and lateral resolution.

Resulting images are shown in **Figures 7.3** through **7.7**.

It seemed initially that the shear-force signal was indeed showing a triple-banding pattern, as previously observed. The imaging of further myofibrils, however, revealed the banding seen in the current experiments to be artifactual; the banding pattern did not vary with bundle size or orientation (cf. **Figure 7.4**). The banding is likely due to subtle alterations in the optical path of the new shear force system introduced by raster scanning of the glass cuvette through which the transverse beam passes.

The current shear force system achieves similar performance to that of Seibel (1996) as judged by comparison of approach curves over glass (cf. **Figure 3.7**). It is therefore likely that if the triple-banding pattern were mechanical as opposed to optical in origin, the pattern would appear superimposed upon the background found herein. No such pattern was seen, arguing against stiffness variation as causative of the pattern.

The sensitivity of image quality to probe-sample distance is shown in **Figures 7.3a, 7.3b**, and **7.3c**. Respective scans at approximately 330, 13 and -150 nm (the latter corresponding to compression of the bundle) from the myofibril bundle surface are shown.

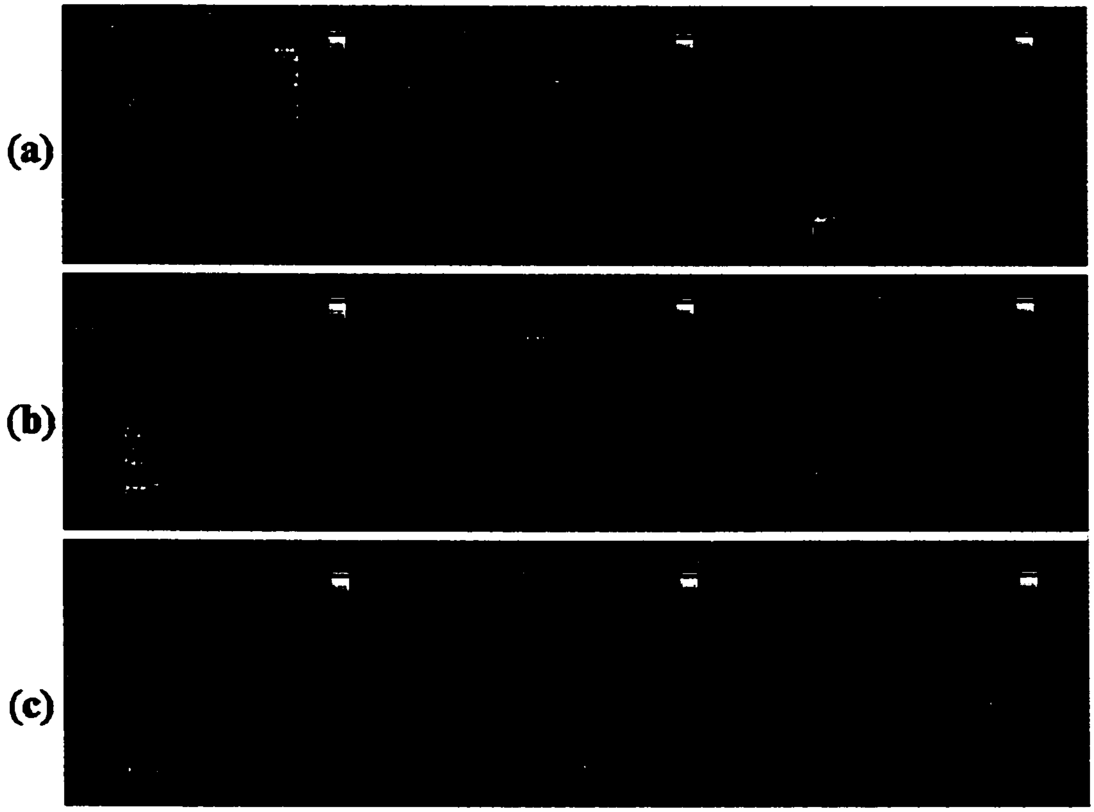

Figure 7.3. Thick myofibril bundle planar scans at varying heights. Scans at approximately 330, 13, and -150 nm from the surface of a bundle of myofibrils (the latter corresponding to compression of the bundle) are shown in (a), (b) and (c), respectively. As the bundle is approached over this ~ 500 nm range, the absorbance image ("PMT corrected sum") becomes more distinct and the high-SSFA bands in the FANSOM image ("SSFA image") become more sharply localized to the I-bands of the bundle. The shear-force image ("Shear") displays banding later determined to be independent of the sample imaged, only coincidentally yielding ~ 3 bands per sarcomere. The bundle-water interface proved too compliant for shear-force detection. SSFA values reflect correction as discussed in Section 7.1. Pixel size is 150 nm (image is ~ 10 µm wide and ~ 8 µm high).

Figure 7.4. Thick myofibril bundle planar scan, rotated orientation. A myofibril bundle similar to that of Figure 7.3 but with an orientation approximately 90° different was located and scanned. The shear-force image shows banding essentially identical to that of the previous images, suggesting an artifactual origin of the shear-force bands observed herein. The bright bands of the SSFA image seem to correspond to the A-bands of the absorbance image. It is likely that the scan grazed the surface of the bundle, as some streaking characteristic of the snaking raster pattern used is evident. The images in this figure are averages of 7 successive scans. Pixel size is 150 nm (image is ~ 10 μm wide and ~ 10 μm high).

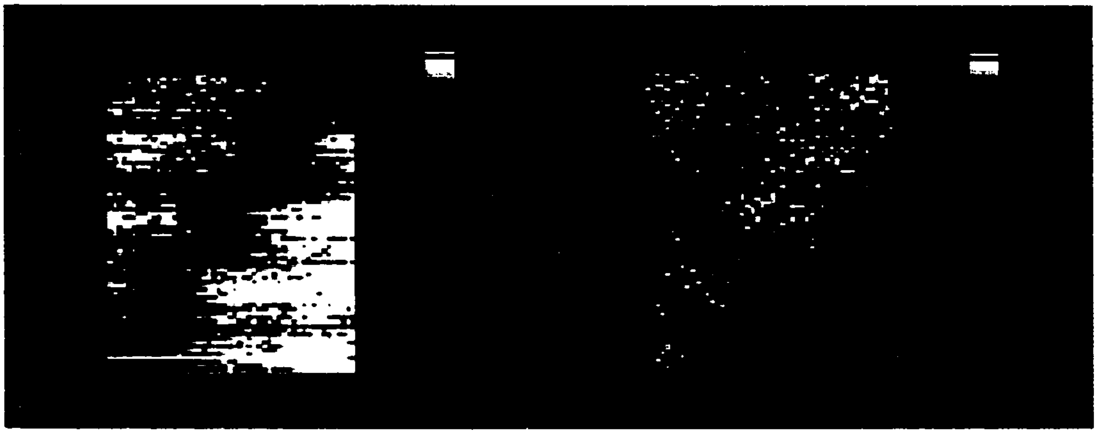

Figure 7.5. Narrow myofibril bundle planar scan. A different myofibril bundle with an orientation similar to that of Figure 7.4 was located and scanned. SSFA image bands seem again to correspond to A-bands. Pixel size is 200 nm (image is ~ 10 μm wide and ~ 15 μm high).

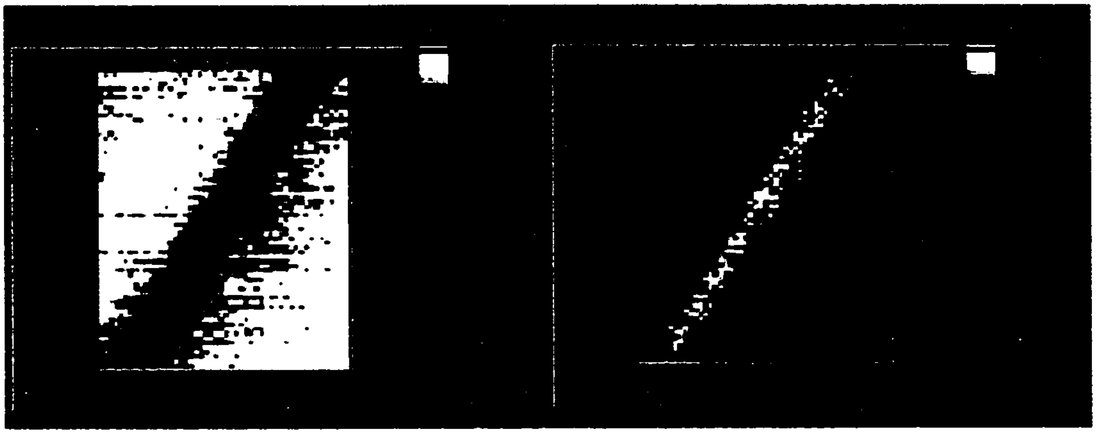

Figure 7.6. Narrow myofibril bundle planar scan, repeated. Another narrow myofibril bundle with a similar orientation to that of Figure 7.5 was scanned from a greater height to reduce raster pattern image streaking. While the resolution is correspondingly reduced, SSFA contrast appears similar to that of Figure 7.5. A greater amount of background is included in the scan, showing that anomalous, negative SSFA values are found as far as ~ 5 diameters from the myofibril, arguing against sample birefringence as the sole origin of this phenomenon. The images in this figure are averages of 10 successive scans. Pixel size is 300 nm (image is ~ 15 μm wide and ~ 20 μm high).

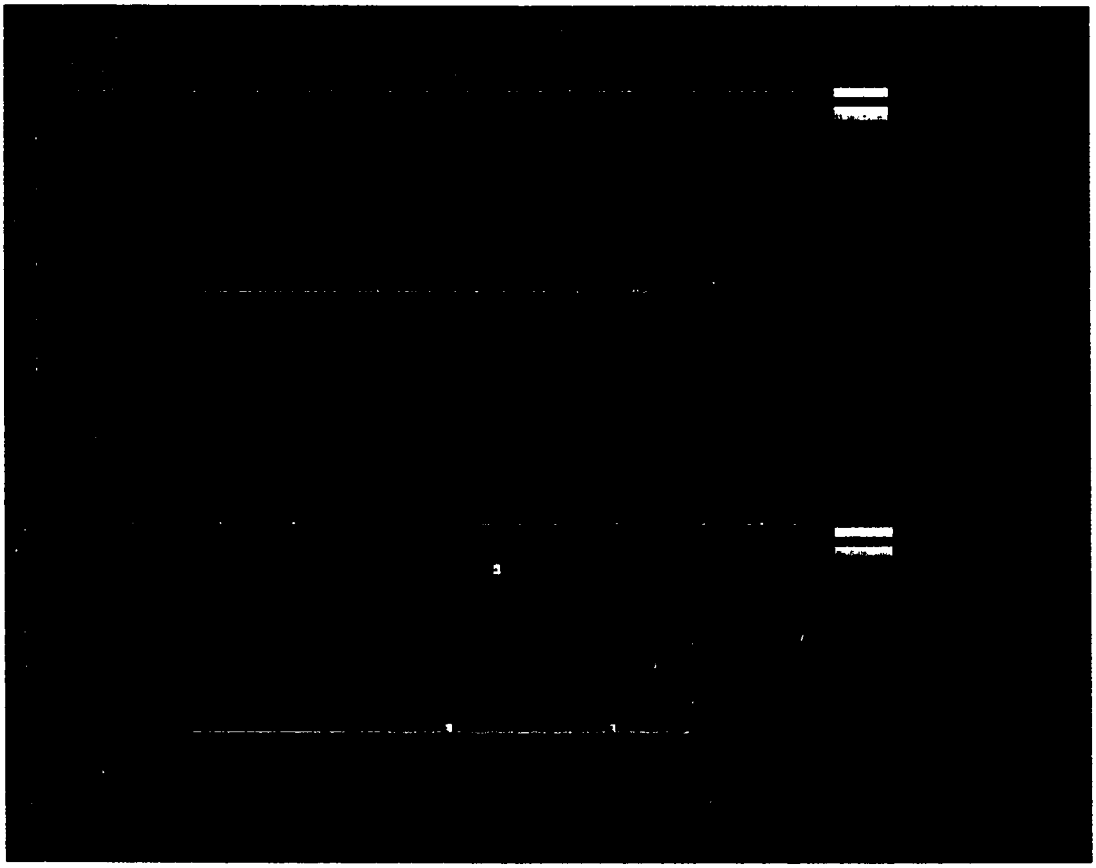

Figure 7.7. Narrow myofibril bundle planar scan, reversed contrast. A further myofibril bundle was located and scanned with the illuminating polarization and polarizing beamsplitter rotated ~ 30° clockwise with respect to the image as viewed, bringing its orientation relative to the illumination into approximate register with that of Figures 7.4 through 7.6. The contrast in the SSFA image appears to be reversed, with anomalously high SSFA values across the field, again suggesting error apart from that of sample birefringence. SSFA image bands appear darker on the whole than their surroundings, with lighter regions corresponding to I-bands, as was seen in Figure 7.3. The images in this figure are averages of 5 successive scans. Pixel size is 300 nm (image is ~ 21 μm wide and ~ 6 μm high).

Only moderate change is evidenced over a range of ~ 500 nm, suggesting a significant contribution of far-field light even upon contact.

The absorbance images (labeled "PMT corrected sum" in the Figures) are formed by the G-weighted sum of both PMT channels (i.e. the measured light intensity in the parallel channel plus that of the perpendicular channel weighted by the differential sensitivity factor G). These show a single, large, relatively opaque band per sarcomere, presumably indicating the A-band region of the bundle. The steady-state fluorescence anisotropy images (labeled "SSFA" in the figures) also showed a single maximum per sarcomere. That the peaks were not found to be tri-modal further argues against viscosity variations as causative of the triple-banding pattern of Seibel (1996).

In **Figure 7.3**, the SSFA maxima occurred between these A-band regions, thus likely corresponding to the I-band and Z-line regions. This relationship was opposite that in **Figures 7.4** through **7.6**. This inconsistency suggests a significant contribution by myofibril birefringence to this pattern, as microviscosity would not be expected to vary with myofibril orientation.

The myofibril bundle of **Figure 7.7**, however, also shows the reversed contrast of **Figure 7.3**, while having the same orientation relative to the illuminating polarization as the myofibrils of **Figures 7.4** through **7.6**. One hypothesis is that the thickness of the bundle of **Figure 7.7**, given the birefringence(s) of the myofibrils, coincided with that necessary to effectively form a half-wave plate, rotating the polarization of the illumination. That the contrast does not appear to vary with the radial variation in bundle thickness, however, argues against this possibility.

A more likely possibility is systematic error in the determination of the differential channel sensitivity G, creating errors as described in Section 4.2. In most of the bundle scans, anomalous apparent SSFA values were found (i.e., far from the value of ~ 0.05 expected from the probe in a simple aqueous solution). This deviation is indicative of either error in the estimation of G, rotation of the axis of light polarization by the myofibrils, or both. In most of the images, the bundle occupied most of the field of view, leaving the source of the error ambiguous. **Figure 7.6**, however, includes several bundle diameters of surrounding background, in which the apparent SSFA remains negative, suggesting that misestimation of G was primarily responsible for the anomalies.

Small (~ 0.1) manual adjustments in G were found able to restore the apparent SSFA measurements to expected values, as was done in **Figure 7.3**. One possible source of this error seemingly peculiar to the myofibril experiments is the requirement of an aqueous environment upon the introduction of the sample to the system. The curved meniscus of the buffer surface could introduce undesired lensing and/or reflections, influencing the measured value of G.

While the myofibril proved to be a more difficult sample of investigation than was anticipated, valuable preliminary information regarding the current lateral resolution of FANSOM and the complexities introduced by sample birefringence was obtained.

In sum, these data suggest that

- sample birefringence and geometry must be well characterized if FANSOM, as implemented, is to yield a quantitative measure of microviscosity independent of the optical properties of the sample
- the triple-banding pattern previously seen in shear-force images of myofibril bundles probably arose from an optical rather than mechanical basis, and
- if external myofibrillar surfaces modify the microviscosity of surrounding water, it is to an extent smaller than ~ 0.1 cp over a range of ~ 1 micron (cf. Section 6.2).

8. Future directions

8.1 Instrumentation upgrades

In the development process, several potential improvements became self-evident, the most important of which would be the use of a calcite-based polarizing beamsplitter, with which channel cross-talk may be reduced 100-fold, improving also the reliability with which the differential channel sensitivity G might be determined. Other potential upgrades include compilation of the software for faster scanning, the use of a contrast-based auto-focusing mechanism to maintain confocality, and "noise-eater" circuitry for the laser used.

A direction of particular interest, as mentioned previously, will be the further development of the heart of the FANSOM system, the chosen molecular probe. An intriguing, albeit currently expensive possibility is the use of Green Fluorescent Protein (GFP). In addition to its spectral similarity to fluorescein, GFP offers a probe with an intimately fixed relationship between the excitation dipole direction and that of the protein as a whole. More immediate possibilities include the use of larger dextrans, the internal crosslinking of the dextrans for greater rigidity, or, more ambitiously, attachment of the fluorophore to the macromolecule via more than one bond.

Also, deconvolution could improve vertical resolution, which will become increasingly important as smaller-scale viscous effects are sought (such as classically predicted surface drag; Howard, 1996). The ion-milling of probe endings, while labor intensive, might then become worthwhile, as the increased ideality of such probes would lend themselves to such mathematical characterization and corrections (Veerman et al., 1999).

The need for such measures might be obviated, however, by a reflection-mode geometry of the microscope. In such an implementation, light would be collected by the probe used for excitation, and this light would be separated from the excitation light by a fiber optic circulator and analyzed. While non-trivial to implement, this modality represents the ultimate in NSOM confocality, virtually eliminating concerns of background fluorescence and focus adjustment.

8.2 Experimental possibilities

Likely next experiments will seek to elucidate the cause of the apparently increased viscosity at the mica surface. Is the viscosity change sensitive to chaotropes? Are molecular probes of different sizes differentially excluded from the surface? Can the range be reduced by bending and/or reducing the size of the mica sheet used?

The high resolution of FANSOM suggests the measurement of fluorescence anisotropy in new situations. How does viscosity vary within the cell? Within a mitochondrion?

With some of the speed and performance enhancements noted above, a wider range of biological questions may be addressed. Are glycolytic enzymes less rotationally free near cytoskeletal filaments? What is the 3-dimensional viscosity profile around a mast cell? How does this profile change upon stimulation of secretion?

Or, implemented in a reflection mode, the probe tip could be freed from bulky hardware, yielding a viscosity probe that can be fed through the smallest gauge of needles, further extending the range of milieu in which viscosity and/or the rotational freedom of molecules may be assayed. Does membrane fluidity vary between tissue types as measured *in situ* by the SSFA of autofluorescent components?

Virtually all binding interactions are accompanied by a change in rotational freedom. This fact, in addition to the ubiquity of viscosity as a fundamental physical parameter, makes the extension of fluorescence anisotropy to small scales a highly promising direction.

The future utility of the technique described herein appears great.

References

- Andrews, P. R., Craik, D. J., and Martin, J. L. (1984) Functional group contributions to drug-receptor interactions. J. Med. Chem. 27:1648-1657.
- Axelrod, D. (1989) Fluorescence polarization microscopy. Meth. Cell Biol. 30:333-352.
- Barenz, J., Hollricher, O., and Marti, O. (1996) An easy-to-use non-optical shear-force distance control for near-field optical microscopes. Rev. Sci. Instrum. 67:1912-1916.
- Bartoo, M. L., Popov, V. I., Fearn, L. A., and Pollack, G. H. (1993) Active tension generation in isolated skeletal myofibrils. J. Muscle Res. Cell Motil. 14:495-510.
- Betzig, E., Finn, P. L., and Weiner, J. S. (1992) Combined shear force and near-field scanning optical microscopy. Appl. Phys. Lett. 60:2484-2486.
- de Bruijn, H. E., Kooyman, R. P. H., and Greve, J. (1992) Choice for metal and wavelength for surface-plasmon resonance sensors: some considerations. Appl. Optics 31:440-442.
- Bukofsky, S. J., and Grober, R. D. (1997) Video rate near-field scanning optical microscopy. 71:2749-2751.
- Cleveland, G. G., Chang, D. C., Hazlewood, C. F., Rorschach, H. E. (1976) Nuclear magnetic resonance measurement of skeletal muscle: anisotropy of the diffusion coefficient of the intracellular water. Biop. J. 16:1043-1053.
- Cline, J. A., Barshatzky, H., and Isaacson, M. (1991) Scanned-tip reflection-mode near-field scanning optical microscopy. Ultramicroscopy 38:299-304.
- Davy, S., Spajer, M., and Courjon, D. (1998) Influence of the water layer on the shear force damping in near-field microscopy. Appl. Phys. Lett. 73:2594-2596.
- Derbyshire, W. and Duff, I. D. (1974) NMR of Agarose Gels. Faraday Discuss. Chem. Soc. 57:243-254.

- Dix, J. A., and Verkman, A. S. (1990) Mapping of fluorescence anisotropy in living cells by ratio imaging. Application to cytoplasmic viscosity. Biophys. J. 57:231-240.
- Durkan, C., and Shvets, I. V. (1996) Investigation of the physical mechanisms of shear-force imaging. J. Appl. Phys. 80:5659-5664.
- Gheber, L. A., Hwang, J. and Edidin, M. (1998) Design and optimization of a near-field scnaning optical microscope for imaging biological samples in liquid. Appl. Optics 37:3574-3581.
- Goodsell, D. S. The machinery of life. Springer-Verlag, New York, 1993.
- Gough, A. H., and Taylor, D. L. (1993) Fluorescence anisotropy imaging microscopy maps calmodulin binding during cellular contraction and locomotion. J. Cell Biol. 121:1095-1107.
- Granath, K. A. (1958) Solution properties of branched dextrans. J. Colloid Sci., 13:308-328.
- Grubb, S. G., Betzig, E., Chichester, R. J., DiGiovanni, D. J., and Weiner, J. S. (1994) Fiber-laser probe for near-field scanning microscopy. Optical Fiber Comm. 4:136.
- Haydon, P. G., Marchese-Ragona, S., Basarsky, T. A., Szulczewski, M., and McCloskey, M. (1996) Near-field confocal optical spectroscopy (NCOS): subdiffraction optical resolution for biological systems. J. Microscopy 182:208-216.
- Hirai, T., personal communication.
- Hoffmann, P., Dutoit, B., and Salathe, R. (1995) Comparison of mechanically drawn and protection layer chemically etched optical fiber tips. Ultramicroscopy 61:165-170.
- Howard, J. PBIO 560 Course notes, UW, Spring 1996.
- Israelachvili, J. and Wennerstrom, H. (1996) Role of hydration and water structure in biological and colloidal interactions. Nature 379:219-225.

- Israelachvili, J. N., and Adams, G. E. (1976) Direct measurement of long range forces between two mica surfaces in aqueous KNO_3 solutions. Nature 262:774-776.
- Israelachvili, J. N., and Adams, G. E. (1978) Measurement of forces between two mica surfaces in aqueous electrolyte solutions in the range of 0-100 nm. J. Chem. Soc. Faraday Trans. 74:975-1001.
- Israelachvili, J. N., and McGuiggan, P. M. (1988) Forces between surfaces in liquids. Science 241:795-800.
- Israelachvili, J. N., and Tabor, D. (1972) Measurement of van der Waals dispersion forces in the range of 1.4 to 130 nm. Nature 236:106.
- Israelachvili, J., Intermolecular and surface forces (Academic Press Inc., San Diego, 1992).
- James, D. R., and Ware, W. R. (1986) Recovery of underlying distributions of lifetimes from fluorescence decay data. Chem. Phys. Lett. 126:7-11.
- Lambelet, P., Sayah, A., Pfeffer, M., Philipona, C., and Marquis-Weible, F. (1998a) Chemically etched fiber tips for near-field optical microscopy: a process for smoother tips. Appl. Optics 37:7289-7292.
- Lambelet, P., Pfeffer, M., Sayah, A., and Marquis-Weible, F. (1998b) Reduction of tip-sample interaction forces for scanning near-field optical microscopy in a liquid environment. Ultramicroscopy 71:117-121.
- Lambooy, P. K., Steiner, R. F., and Sternberg, H. (1982) Molecular dynamics of calmodulin as monitored by fluorescence anisotropy. Arch. Bioc. Biop. 217:517-528.
- Lavalette, D., Tetreau, C., Tourbez, M., and Blouquit, Y. (1999) Microscopic viscosity and rotational diffusion of proteins in a macromolecular environment. Biop. J. 76:2744-2751.
- Luby-Phelps, K., Taylor, D. L., and Lanni, F. (1986) Probing the structure of cytoplasm. J. Cell Biol. 102:2015-2022.

- McDaniel, E. B., McClain, S. C., and Hsu, J. W. P. (1998) Nanometer scale polarimetry studies using a near-field scanning optical microscope. Appl. Optics 37:84-92.
- Muramatsu, H., Homma, K., Chiba, N., Yamamoto, N., and Egawa, A. (1999) Dynamic etching method for fabricating a variety of tip shapes in the optical fibre probe of a scanning near-field optical microscope. J. Microscopy 194:383-387.
- Murase, N., and Watanabe, T. (1989) Nuclear magnetic relaxation studies of the compartmentalized water in crosslinked polymer gels. Mag. Res. in Medicine 9:1-7.
- Okajima, T., and Hirotsu, S. (1997) Study of shear force between glass microprobe and mica surface under controlled humidity. Appl. Phys. Lett. 71:545-547.
- O'Neill, M. P., and Bearden, A. (1995) Laser-feedback measurements of turtle basilar membrane motion using direct reflection. Hearing Research 84:125-138.
- Parson, W. BIOC 562 Course notes, Spring 1993.
- Pavesi, L., and Balzarini, M. (1996) NMR study of the diffusion processes in gels. Mag. Res. Imag. 14:985-987.
- Pollack, G. H. Cells and Gels: Exploring the engines of life (Ebner and sons, Seattle, 2001).
- Seibel, E. (1996) Development of a near-field scanning optical microscope for imaging biological samples in physiological buffer. Doctoral Dissertation, University of Washington.
- Seibel, E. J. and Pollack, G. H. (1997) Imaging 'intact' myofibrils with a near-field scanning optical microscope. J. Microsc. 186:221-231.
- Shin, D. J., Chavez-Pirson, A., and Lee, Y. H. (1999) Diffraction of circularly polarized light from near-field optical probes. J. Microsc. 194:353-359.
- Solomons, T. W. G. Organic Chemistry, 4th ed. John Wiley & Sons, Inc., New York, 1988.

- Steiner, R. F., Lambooy, P. K., and Sternberg, H. (1983) The dependence of the molecular dynamics of calmodulin upon pH and ionic strength. Arch. Bioc. Biop. 222:158-169.
- Stockle, R., Fokas, C., Deckert, V., and Zenobi, R. (1999a) High-quality near-field optical probes by tube etching. Appl. Phys. Lett. 75:160-162.
- Stockle, R., Schaller, N., Deckert, V., Fokas, C., and Zenobi, R. (1999b) Brighter near-field optical probes by means of improving the optical destruction threshold. J. Microscopy 194:378-382.
- Talley, C. E., Cooksey, G. A., and Dunn, R. C. (1996) High resolution fluorescence imaging with cantilevered near-field fiber optic probes. 69:3809-3811.
- Tkach, R. W., and Chraplyvy, A. R. (1986) Regimes of feedback effects in 1.5-um distributed feedback lasers. J. Lightwave. Tech. LT-4:1655-1661.
- van Holde, K. E. Physical Biochemistry, 2nd ed. Prentice-Hall, Englewood Cliffs, 1985.
- Veerman, J. A., Garcia-Parajo, M. F., Kuipers, L., and van Hulst, N. F. (1999) Single molecule mapping of the optical field distribution of probes for near-field microscopy. J. Microscopy 194:477-482.
- Vogler, E. A. (1998) Structure and reactivity of water at biomaterial surfaces. Adv. Colloid Interface Sci. 74:69-117.
- von Freymann, G., Wegener, M., and Schimmel, T. (1999) Depolarization near-field scanning optical microscopy: influence of wavelength and tip shape on the lateral resolution. Surf. Interface Anal. 29:499-502.
- Wiggins, P. M. (1990) Role of water in some biological processes. Microbiol. Rev. 54:432:449.
- Witten, T. A. (1990) Structured fluids. Physics Today 43:21-28.
- Woessner, D. E. and Snowden Jr., B. S. (1970) Pulsed NMR study of water in agar gels. J. Coll. Interface Sci. 34:290-299.

- Xu, X., and Yeung, E. S. (1998) Long-range electrostatic trapping of single-protein molecules at a liquid-solid interface. Science 281:1650-1653.
- Yoshida, A., and Asakura, T. (1974) Electromagnetic field near the focus of gaussian beams. Optik 41:281-292.

Appendix: *SSFA of fluorophores excited by light of a given polarization state*

This derivation closely parallels that for the case of completely polarized excitation by Parson (1993).

The rate at which a population of fluorophores absorbs light is given by

$$\text{rate}_{0\rightarrow a} = (1 / \hbar^2) \mid \mu_{0a} \mid^2 \bullet \mid F_\nu \mid^2 \cos^2\psi\, N_{0.}$$

where $\hbar$ is Planck's constant divided by 2π, μ_{0a} is the dipole moment vector of the fluorophore, F_ν is the electric field vector's frequency ν content, N_0 is the concentration of fluorophores in their ground state, and ψ is the angle between the dipole and field vectors.

The probability of excitation of a fluorophore with a given dipole moment vector by an electric field F_ν is proportional to $\cos^2\psi$. For an electric field comprising two orthogonal polarization components, this probability takes the form

$$P \propto A \cos^2 \psi + B \sin^2 \psi,$$

where P is the probability of excitation and A and B are the electric field amplitudes in the directions parallel and perpendicular to the direction of maximum polarization, respectively.

The fraction of molecules with their dipoles oriented within a given angle range is proportional to the area element $\sin \phi \, d\phi \, d\theta$ on a unit radius sphere. The fraction of excited molecules with this orientation, $W(\phi,\theta)\, d\phi\, d\theta$, is therefore given by:

$$W(\phi,\theta)\cdot d\theta\cdot d\phi=\frac{(A\cos^2\phi+B\sin^2\phi)\cdot\sin\phi\cdot d\theta\cdot d\phi}{\int_0^{\pi}(A\cos^2\phi+B\sin^2\phi)\cdot\sin\phi\cdot d\phi\cdot\int_0^{2\pi}d\theta}$$

The denominator simply counts all excited molecules. Evaluating the denominator

$$\begin{aligned}&\int_0^{\pi}(A\cos^2\phi+B\sin^2\phi)\cdot\sin\phi\cdot d\phi\cdot\int_0^{2\pi}d\theta\\&=((-A/3)\cos^3\phi+(B/3)\sin^2\phi\cos\phi-(2B/3)\cos\phi)\Big|_0^{\pi}\cdot2\pi\\&=\frac{4}{3}\pi\cdot(A+2B)\end{aligned}$$

gives

If the molecules then emit photons parallel to their dipole moments without reorientation, the component $F\parallel$ of fluorescence polarized parallel to the direction of maximum excitation polarization is given by

$$\begin{aligned}&F\parallel=\int_0^{2\pi}d\theta\cdot\int_0^{\pi}W(\phi,\theta)\cdot\cos^2\phi\cdot d\phi\\&=\frac{2\pi A}{K}(1/5)\cos^5\phi\Big|_0^{\pi}+\frac{2\pi B}{K}((1/5)\sin^2\phi\cos^3\phi-(2/5)\cos^3\phi))\Big|_0^{\pi}\\&=\frac{4\pi}{5K}\cdot(A+\frac{2}{3}B)\\&=\frac{3\cdot(A+\frac{2}{3}B)}{5\cdot(A+2B)}\end{aligned}$$

where the aforementioned denominator counting all excited molecules is abbreviated as K. Similarly, the component $F\perp$ of fluorescence with perpendicular polarization is given by

$$F\perp=\int_0^{2\pi}\cos^2\theta\cdot d\theta\cdot\int_0^{\pi}W(\phi,\theta)\cdot\sin^2\phi\cdot d\phi$$

$$=\pi\cdot(\frac{A}{K}(\frac{-\sin^2\phi\cdot\cos^3\phi}{5}-\frac{2}{5}\frac{\cos^3\phi}{3})+\frac{B}{K}(\frac{\sin^4\phi\cdot\cos\phi}{5}+\frac{4}{5}\frac{\sin^2\phi\cdot\cos\phi}{3}-\frac{8}{15}\cos\phi))\Big|_0^{\pi}$$

$$=\frac{1}{5}\cdot(\frac{A+4B}{A+2B})$$

The above equations represent the fluorescence obtained in the absence of fluorophore reorientation, and therefore give maximum values. The maximum fluorescence anisotropy obtainable given excitation light of arbitrarily polarization is therefore

$$r_0=\frac{\dfrac{3\cdot(A+\frac{2}{3}B)}{5\cdot(A+2B)}-\dfrac{1}{5}\cdot(\dfrac{A+4B}{A+2B})}{\dfrac{3\cdot(A+\frac{2}{3}B)}{5\cdot(A+2B)}+\dfrac{2}{5}\cdot(\dfrac{A+4B}{A+2B})}$$

$$=0.4\cdot\frac{(A-B)}{(A+2B)}$$

In the case of completely polarized excitation (i.e., A = 1, B = 0), these relations reduce to the more familiar

$$F\| = 3/5,$$

$$F\perp = 1/5,$$

and

$$r_0 = 0.4.$$

Frederick B. Reitz

Education:

University of Washington, B.S.E.E., 1991, Electrical Engineering
University of Washington, Ph.D., 2001, Bioengineering

Research Experience:

7/86	Summer research on the National Synchrotron Light Source UV and X-ray rings at Brookhaven National Laboratory, Long Island, NY
4/92-5/96	Graduate Research Assistant, Laboratory of Leonard Pagliaro, UW Bioengineering (research on glycolytic enzyme organization; involved protein isolation, cell culture, fluorescent analog preparation, microinjection, ratio imaging, fluorescence redistribution after photobleaching, viscometry, image processing, epi-fluorescence and phase microscopy, SDS-PAGE, column chromatography, high pressure chamber design)
8/94	Post-course research with Edward Salmon, Ph.D. on artificial cleavage furrow induction in sea urchin eggs (*Arbacia punctulata*), Physiology Course, Marine Biological Laboratory, Woods Hole, MA
6/94-7/94	Student, Physiology Course, Marine Biological Laboratory, Woods Hole, MA
8/99	Silicon nitride nanolever microfabrication at Cornell Nanofabrication Facility
6/96-3/01	Graduate Research Assistant, Laboratory of Gerald Pollack, UW Bioengineering (development of fluorescence anisotropy near-field scanning optical microscopy system for microviscometric use)
3/01-pres.	Postdoctoral Fellow, Laboratory of Gerald Pollack, UW Bioengineering

Leadership Experience:

1/93-3/93	Graduate Teaching Assistant, Digital Electronics, incl. Laboratory (BIOEN 535)
4/93-6/93	Graduate Teaching Assistant, Biomedical Light Microscopy and Imaging, incl. Laboratory (BIOEN 599E)
9/93-6/94	Bioengineering representative to the University of Washington Graduate and Professional Student Senate
12/95-5/96	Mentor, University of Washington Undergraduate Research Program, Directed two undergraduate students in research on glucokinase and glucokinase regulatory protein localization (involving protein purification, cell culture and immunological techniques)
10/98-12/98	Participant, Leadership Skills Training, Context Associated, Seattle, WA
6/99-3/00	Mentor, University of Washington Undergraduate Research Program, Directed an undergraduate student in the development and implementation of aluminum coating system and laser-feedback experimentation

Honors and Awards:

1986	Brookhaven National Laboratory National High School Honors Research Program (selected to represent Washington State)
1987	National Merit Scholar
1990-91	Chevron Scholarship
1994	Tuition Fellowship, Physiology Course, Marine Biological Laboratory, Woods Hole, MA.
1994	Society of General Physiologists Scholar (for outstanding performance in MBL Physiology Course)
1997-99	UW Center for Nanotechnology Fellow

Papers:

- Reitz, F. B. & Pollack, G. H. (2001) Fluorescence Anisotropy Near-field Scanning Optical Microscopy (FANSOM): A new technique for nano-scale microviscometry. *(submitted to Ultramicroscopy)*
- Reitz, F. B. & Pollack, G. H. (2001) Labview Virtual Instruments for Calcium Buffer Calculations, *(submitted to Computer Methods and Programs in Biomedicine)*
- Sokolov, S. Yu., Grinko, A. A., Tourovskaia, A. V., Reitz, F. B., Pollack, G. H., & Blyakhman, F. A. (1999) "Minimum average risk" as a new peak detection algorithm applied to myofibrillar dynamics. *(submitted to IEEE Transactions)*
- Reitz, F. & Pagliaro, L. (1997) Does regulatory protein play a role in glucokinase localization? Horm. Metab. Res. 29:317-321.
- Pagliaro, L., Wang, J. & Reitz, F. (1995) A high numerical aperture miniature optical pressure chamber for use with adherent mammalian cells. Undersea & Hyperbaric Med. 22:171-181.
- Reitz, F. B. & Pagliaro, L. (1994) Fiber optic scrambling in light microscopy: A computer simulation and analysis. J. Microscopy. 176:143-151.
- Wang, J., Reitz, F., Donaldson, T. & Pagliaro, L. (1994) A computer-interfaced falling ball viscometer. J. Biophys. Biochem. Meth. 28:251-261.

Other Publications:

- Pollack, G. H., and Reitz, F. B. Phase transitions and molecular motion in the cell. Book chapter, submitted.
- Pollack, G. H., Blyakhman, F. A., Reitz, F. B., Yakovenko, O. V. & Dunaway, D. L. Natural muscle as a biological system. Book chapter, submitted.
- Ratio image of labeled glucokinase and size-matched dextran in a cultured rat insulinoma (RIN-5AH) cell for the cover of the July 1997 issue of Horm. Metab. Res.
- Reitz, F. B., Wang, J. & Pagliaro, L. (1994) A fraction of glucokinase is bound in living 3T3 cells. Mol. Biol. Cell 5:419a.
- Wang, J., Reitz, F. & Pagliaro, L. (1994) Probing enzyme organization in living cells with low light level fluorescence microscope imaging and photobleaching. Annals of Biomed. Engineering 22:37.